

MIT Open Access Articles

Discovery and Identification of MAXI J1621–501 as a Type I X-Ray Burster with a Super-orbital Period

The MIT Faculty has made this article openly available. **Please share** how this access benefits you. Your story matters.

As Published: 10.3847/1538-4357/AB3E43

Publisher: American Astronomical Society

Persistent URL: <https://hdl.handle.net/1721.1/136565>


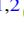





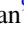
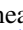
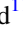








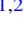
Version: Final published version: final published article, as it appeared in a journal, conference proceedings, or other formally published context

Terms of Use: Article is made available in accordance with the publisher's policy and may be subject to US copyright law. Please refer to the publisher's site for terms of use.





Discovery and Identification of MAXI J1621–501 as a Type I X-Ray Burster with a Super-orbital Period

Nicholas M. Gorgone^{1,2} , Chryssa Kouveliotou^{1,2} , Hitoshi Negoro³, Ralph A. M. J. Wijers⁴ , Enrico Bozzo⁵ , Sylvain Guiriec^{1,2} , Peter Bult⁶, Daniela Huppenkothen⁷ , Ersin Göğüş⁸ , Arash Bahramian⁹ , Jamie Kennea¹⁰ , Justin D. Linford^{11,12} , James Miller-Jones⁹ , Matthew G. Baring¹³, Paz Beniamini^{1,2} , Deepto Chakrabarty¹⁵ , Jonathan Granot^{1,16} , Charles Hailey¹⁷, Fiona A. Harrison¹⁴, Dieter H. Hartmann¹⁸ , Wataru Iwakiri¹⁹, Lex Kaper⁴, Erin Kara²⁰, Simona Mazzola²¹, Katsuhiro Murata²², Daniel Stern²³ , John A. Tomsick²⁴ , Alexander J. van der Horst^{1,2} , and George A. Younes^{1,2} 

¹ Department of Physics, The George Washington University, Washington, DC 20052, USA

² Astronomy, Physics and Statistics Institute of Sciences (APSiS), The George Washington University, Washington, DC 20052, USA

³ Department of Physics, Nihon University, 1-8 Kanda-Surugadai, Chiyoda-ku, Tokyo 101-8308, Japan

⁴ University of Amsterdam, Science Park 904, 1098 XH Amsterdam, The Netherlands

⁵ University of Geneva, Chemin d'Ecogia 16, Versoix, 1290 Switzerland

⁶ Astrophysics Science Division, NASA's Goddard Space Flight Center, Greenbelt, MD 20771, USA

⁷ DIRAC Institute, Department of Astronomy, University of Washington, 3910 15th Avenue NE, Seattle, WA 98195, USA

⁸ Faculty of Engineering and Natural Sciences, Sabanci University, Orhanlı-Tuzla 34956, İstanbul, Turkey

⁹ International Centre for Radio Astronomy Research—Curtin University, GPO Box U1987, Perth, WA 6845, Australia

¹⁰ The Pennsylvania State University, University Park, PA 16802, USA

¹¹ Department of Physics and Astronomy, West Virginia University, P.O. Box 6315, Morgantown, WV 26506, USA

¹² Center for Gravitational Waves and Cosmology, West Virginia University, Chestnut Ridge Research Building, Morgantown, WV 26505, USA

¹³ Physics and Astronomy Department, Rice University, 6100 Main Street, Houston, TX, USA

¹⁴ Cahill Center for Astrophysics, California Institute of Technology, 1216 East California Boulevard, Pasadena, CA 91125, USA

¹⁵ MIT Kavli Institute for Astrophysics and Space Research, Massachusetts Institute of Technology, Cambridge, MA 02139, USA

¹⁶ Department of Natural Sciences, The Open University of Israel, P.O. Box 808, Ra'anana 43537, Israel

¹⁷ Columbia Astrophysics Laboratory, Columbia University, New York, NY 10027, USA

¹⁸ Department of Physics and Astronomy, Clemson University, Kinard Lab of Physics, Clemson, SC 29634-0978, USA

¹⁹ Department of Physics, Faculty of Science and Engineering, Chuo University, 1-13-27 Kasuga, Bunkyo-ku, Tokyo 112-8551, Japan

²⁰ Department of Astronomy, University of Maryland, College Park, MD 20742, USA

²¹ Dipartimento di Fisica e Chimica—Emilio Segrè, Università degli Studi di Palermo, Via Archirafi 36-I-90123 Palermo, Italy

²² Department of Particle and Astrophysical Science, Nagoya University, Furo-cho, Chikusa-ku, Nagoya, 464-8602, Aichi, Japan

²³ Jet Propulsion Laboratory, California Institute of Technology, 4800 Oak Grove Drive, Mail Stop 169-221, Pasadena, CA 91109, USA

²⁴ Space Sciences Laboratory, 7 Gauss Way, University of California, Berkeley, CA 94720-7450, USA

Received 2019 June 27; revised 2019 August 15; accepted 2019 August 21; published 2019 October 22

Abstract

MAXI J1621–501 is the first *Swift*/XRT Deep Galactic Plane Survey transient that was followed up with a multitude of space missions (*NuSTAR*, *Swift*, *Chandra*, *NICER*, *INTEGRAL*, and MAXI) and ground-based observatories (*Gemini*, IRSF, and ATCA). The source was discovered with MAXI on 2017 October 19 as a new, unidentified transient. Further observations with *NuSTAR* revealed two Type I X-ray bursts, identifying MAXI J1621–501 as a low mass x-ray binary with a neutron star primary. Overall, 24 Type I bursts were detected from the source during a 15 month period. At energies below 10 keV, the source spectrum was best fit with three components: an absorbed blackbody with $kT = 2.3$ keV, a cutoff power law with index $\Gamma = 0.7$, and an emission line centered on 6.3 keV. Timing analysis of the X-ray persistent emission and burst data has not revealed coherent pulsations from the source or an orbital period. We identified, however, a super-orbital period ~ 78 days in the source X-ray light curve. This period agrees very well with the theoretically predicted radiative precession period of ~ 82 days. Thus, MAXI J1621–501 joins a small group of sources characterized with super-orbital periods.

Unified Astronomy Thesaurus concepts: [Low-mass X-ray binary stars \(939\)](#); [X-ray transient sources \(1852\)](#); [X-ray bursters \(1813\)](#)

1. Introduction

Low-mass X-ray binaries (LMXBs) consist of a compact object, either a neutron star (NS) or a black hole (BH), and a donor star, typically a late-type, low-mass main-sequence star. Most LMXBs are persistent X-ray sources, as mass transferred through Roche lobe overflow from the donor to the compact object efficiently converts its gravitational potential energy to X-rays (Remillard & McClintock 2006; Done et al. 2007). Several LMXBs exhibit transient outbursts, during which their X-ray luminosities increase by orders of magnitude; such outbursts generally last anywhere between a couple of weeks to months. Identifying the nature of the compact object, namely

whether it is an NS or a BH, through data collected during the outburst, is usually a nontrivial task. However, the detection of type I X-ray bursts from the compact object unambiguously identifies it as an NS. Type I X-ray bursts are thermonuclear explosions; they take place on the surface layers of the NS when the accreted He or H from the companion star reaches the critical density to initiate nuclear fusion, resulting in a He flash.

About ~ 30 transient LMXBs have exhibited multiperiodic rebrightening during their outbursts, known as “super-orbital periods” or long periods. These are not strictly periodic and they are likely due to a long period present in the system (Gerend & Boynton 1976) produced by the accretion disk

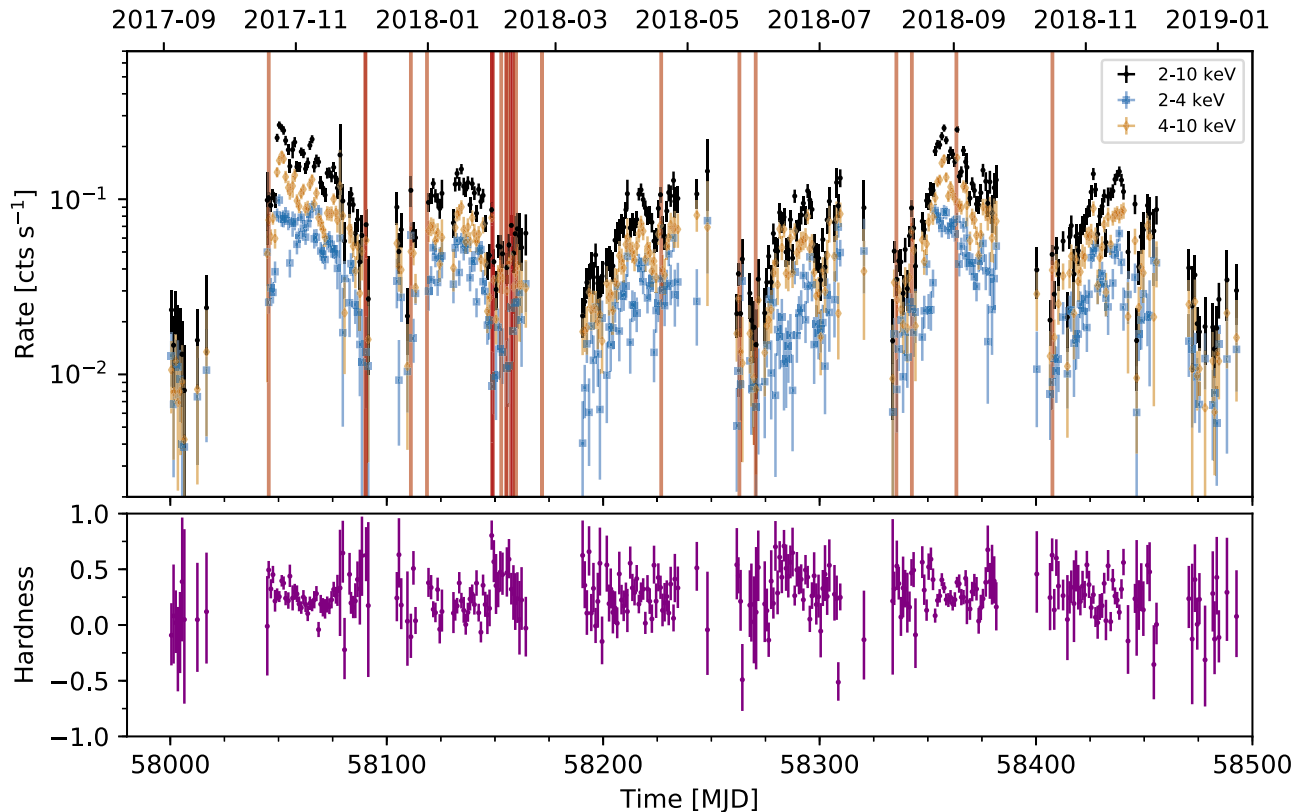


Figure 1. Top: MAXI light curve of J1621 plotted in the 2.0–10.0 keV (black points), 2.0–4.0 keV (S, blue squares), and 4.0–10.0 keV (H, orange diamonds) bands. Red vertical lines indicate the observation time of an X-ray burst from any instrument. Bottom: hardness ratio = $(H-S)/(H+S)$ for each point in the light curve.

when a torus of disk material precesses retrogradely. The warped disk can reflect or obscure light from the accretor, depending on its orientation (see Figures 7 and 10 of Wijers & Pringle 1999, hereafter WP99). J1621 exhibits such a long period, which we discuss in Section 5.

On 2017 October 19, the Monitor of All-sky X-ray Image (MAXI) Nova Alert System (Negoro et al. 2016; Hashimoto et al. 2017) was activated by a new transient designated as MAXI J1621–501 (hereafter J1621). This observation was followed up with a *Neil Gehrels Swift Observatory* (hereafter *Swift*) target of opportunity (ToO) observation to localize the source, which fell within the survey area of the *Swift*/XRT Deep Galactic Plane Survey (DGPS). The DGPS is a *Swift* and *NuSTAR* legacy project designed to systematically search for transients within the Galactic boundaries of $|b| < 0.5^\circ$, $10^\circ < |l| < 30^\circ$ (initial phase, PI: C. Kouveliotou; Gorgone et al. 2017a). J1621 is the first new source classified with the DGPS.

The *Swift* and *INTEGRAL* teams initiated monitoring campaigns of J1621 soon after its discovery, which were interspersed with multiwavelength ToO requests. X-ray observations were interrupted for a 2.5 month long period (late 2017 October to mid 2018 January) due to Sun constraints. MAXI and *Swift*/XRT resumed monitoring thereafter; thus far, J1621 has exhibited a series of six weaker outbursts (Figure 1). The MAXI data show that the source activity subsided as of 2019 March, returning to its quiescent count rate $\sim 10^{-2}$ counts s^{-1} .

In early 2017 December, we activated the *NuSTAR* legacy program to observe J1621. These observations revealed two type I X-ray bursts, enabling the concrete identification of J1621 as a type I X-ray burster. Further observations with

INTEGRAL, MAXI, and the *Neutron Star Interior Composition Explorer* (*NICER*), detected a total of 24 bursts. In early 2018 March we observed and accurately localized the source with our *Chandra* ToO observation. The *Chandra* location enabled the solid identification of a near-IR counterpart in our *Gemini* follow-up observations, which was clearly brighter than its likely quiescent state as observed in archival data (A. Bahramian et al. 2019, in preparation).

We describe below our comprehensive, 15 month long X-ray campaign monitoring the outburst of J1621 as well as our multiwavelength searches during this interval. In Section 2 we discuss the observations and the data processing, and in Section 3 we describe the spectral and temporal results of the source persistent emission. We present a detailed analysis of 3 out of the 24 type I X-ray bursts (Bult et al. 2017; Chenevez et al. 2018) in Section 4. We discuss our results in Section 5.

2. Observations and Data Processing

We observed J1621 with multiple X-ray missions (*NuSTAR*, *Swift*, *Chandra*, *NICER*, *INTEGRAL*, and MAXI) to trace the X-ray temporal and spectral evolution throughout its outburst. For the localization of the source X-ray counterpart we employed our ToO observation with *Chandra*/HRC-I, which led to confirmation of its near-IR counterpart with *Gemini*. We also utilized *Swift*/UVOT and InfraRed Survey Facility (IRSF) observations, as well as observations at longer wavelengths with the Australia Telescope Compact Array (ATCA). We describe below our observations and data processing for each instrument. Table 1 lists the timeline of all observations per instrument.

Table 1
Observations of MAXI J1621–501 in Chronological Order

Obs.	ID	Mission	Telescope/Mode	Start Time (UT) (dd Mmm yyyy hh:mm)	Exposure (ks)	References
1. ^b	...	MAXI	GSC	2017 Oct 19 05:45	^a	[1]
2.	00010351007	<i>Swift</i>	XRT/PC + UVOT	2017 Oct 19 18:09	0.1	[2]
3.	00010352001	<i>Swift</i>	XRT/PC + UVOT	2017 Oct 19 18:11	0.4	[2]
4.	00010357001	<i>Swift</i>	XRT/PC + UVOT	2017 Oct 19 19:17	0.5	[2]
5.	00036140002	<i>Swift</i>	XRT/WT + UVOT	2017 Oct 20 20:39	1.0	This work
6.	1020630101	<i>NICER</i>	XTI	2017 Oct 21 14:24	0.1	This work
7.	GS-2018A-DD-201	<i>Gemini</i>	FLAMINGOS-2	2017 Oct 21 23:37	^c	[3]
8.	00036140003	<i>Swift</i>	XRT/WT	2017 Oct 22 01:56	0.4	This work
9.	1020630102	<i>NICER</i>	XTI	2017 Oct 22 09:25	0.6	This work
10.	...	IRSF	SIRIUS	2017 Oct 22 17:44	0.3	This work
11.	00036140004	<i>Swift</i>	XRT/WT + UVOT	2017 Oct 24 04:35	1.1	This work
12.	90301322001	<i>NuSTAR</i>	FPMA/B	2017 Oct 26 00:46	38.3	This work
13.	00087355002	<i>Swift</i>	XRT/PC + UVOT	2017 Oct 26 07:25	0.6	[4]
14.	CX399	ATCA	5.5, 9 GHz	2017 Nov 18 19:00	18.0	This work
15. ^b	9030132800[1/2]	<i>NuSTAR</i>	FPMA/B	2017 Dec 02 23:06	39.0	[5]
16.	9030132800[3/4]	<i>NuSTAR</i>	FPMA/B	2017 Dec 03 15:16	10.0	This work
17.	00036140006	<i>Swift</i>	XRT/WT + UVOT	2018 Jan 13 11:47	0.9	This work
18.	00036140007	<i>Swift</i>	XRT/WT + UVOT	2018 Jan 20 19:05	0.9	This work
19.	00036140008	<i>Swift</i>	XRT/WT + UVOT	2018 Jan 27 00:51	1.0	This work
20. ^b	...	<i>INTEGRAL</i>	ISGRI/JEM-X(1 and 2)	2018 Jan 27 14:29	^a	[6]
21.	00036140009	<i>Swift</i>	XRT/WT	2018 Feb 03 03:44	1.0	This work
22.	00036140011	<i>Swift</i>	XRT/PC + UVOT	2018 Feb 08 12:29	1.0	[7]
23.	00036140012	<i>Swift</i>	XRT/WT + UVOT	2018 Feb 10 15:41	0.8	This work
24.	00036140014	<i>Swift</i>	XRT/WT + UVOT	2018 Feb 21 05:57	0.6	This work
25.	20334	<i>Chandra</i>	HRC-I	2018 Feb 22 20:43	2.6	This work
26. ^b	1034170101	<i>NICER</i>	XTI	2018 Feb 22 16:04	5.7	This work
27.	1034170102	<i>NICER</i>	XTI	2018 Feb 22 23:59	0.5	This work
28.	00036140016	<i>Swift</i>	XRT/WT + UVOT	2018 Feb 28 09:16	0.9	This work
29.	1034170103	<i>NICER</i>	XTI	2018 Feb 28 07:49	4.2	This work
30.	1034170104	<i>NICER</i>	XTI	2018 Mar 01 06:58	5.3	This work
31.	1034170105	<i>NICER</i>	XTI	2018 Mar 02 00:02	5.7	This work
32.	1034170106	<i>NICER</i>	XTI	2018 Mar 03 16:01	2.4	This work
33.	1034170107	<i>NICER</i>	XTI	2018 Mar 04 10:32	2.1	This work
34.	1034170108	<i>NICER</i>	XTI	2018 Mar 05 06:43	1.7	This work
35.	1034170109	<i>NICER</i>	XTI	2018 Mar 06 15:08	1.3	This work
36.	00036140017	<i>Swift</i>	XRT/WT + UVOT	2018 Mar 08 21:15	0.8	This work
37.	00036140018	<i>Swift</i>	XRT/WT + UVOT	2018 Mar 10 22:39	1.1	This work
38.	00010670001	<i>Swift</i>	XRT/WT + UVOT	2018 Apr 25 10:42	1.5	This work
39.	00010670002	<i>Swift</i>	XRT/WT + UVOT	2018 Apr 27 12:09	1.1	...
40.	00010670003	<i>Swift</i>	XRT/WT + UVOT	2018 May 02 22:39	0.9	This work
41.	00010670004	<i>Swift</i>	XRT/WT + UVOT	2018 May 09 12:37	0.5	This work
42.	00010670005	<i>Swift</i>	XRT/WT + UVOT	2018 May 17 08:33	0.9	This work
43.	00010670006	<i>Swift</i>	XRT/WT + UVOT	2018 May 23 06:26	1.0	This work
44.	00010670007	<i>Swift</i>	XRT/WT + UVOT	2018 May 30 16:47	0.9	This work
45.	1034170110	<i>NICER</i>	XTI	2018 Jun 02 23:10	0.4	This work
46.	1034170111	<i>NICER</i>	XTI	2018 Jun 03 03:48	0.2	This work
47.	1034170112	<i>NICER</i>	XTI	2018 Jun 05 14:14	1.2	This work
48.	00010670008	<i>Swift</i>	XRT/WT + UVOT	2018 Jun 06 10:02	1.0	This work
49.	00010670009	<i>Swift</i>	XRT/WT + UVOT	2018 Jun 13 04:52	0.03	This work
50.	00010670010	<i>Swift</i>	XRT/WT + UVOT	2018 Jun 18 10:52	0.8	This work
51.	00010670011	<i>Swift</i>	XRT/WT + UVOT	2018 Jun 20 05:43	0.3	This work

Notes.^a Continuous monitoring.^b X-ray bursts detected.^c Exposures are 0.3 ks, 0.1 ks, and 0.3 ks for the *H*, *J*, and *K_s* bands, respectively.**References.** [1] Hashimoto et al. (2017), [2] Bahramian et al. (2017), [3] A. Bahramian et al. (2019, in preparation), [4] Gorgone et al. (2017b), [5] Bult et al. (2017), [6] Chenevez et al. (2018), [7] Gorgone et al. (2018).

2.1. The Monitor of All-sky X-Ray Image (MAXI)

MAXI (Matsuoka et al. 2009) is an all-sky monitor mounted on the Japanese Experimental Module Exposed Facility of the International Space Station (ISS). MAXI covers 85% of the sky at a cadence of ~ 90 minutes. The monitor consists of two instruments, the Solid-state Slit Camera (SSC: 0.7–7 keV; Tomida et al. 2011) and the Gas Slit Camera (GSC: 2–20 keV; Mihara et al. 2011).

To analyze the observations of J1621 we first extracted MAXI/GSC data in the 2–4 keV (soft) and 4–10 keV (hard) bands by using the image fit method (Mori et al. 2016), which takes into account the point-spread functions of the cameras, as well as X-ray contamination from nearby sources. Due to 4U 1624–490 lying $1^{\circ}.49$ away, we only used cameras GSC_2, GSC_4, GSC_5, and GSC_7, which are well-calibrated spatially. We then subtracted the Galactic ridge emission, comprising constant contributions of about 3.2×10^{-3} counts s^{-1} cm^{-2} and 5.2×10^{-3} counts s^{-1} cm^{-2} , and sinusoidal components with amplitudes of 4.0×10^{-3} counts s^{-1} cm^{-2} and 3.5×10^{-3} counts s^{-1} cm^{-2} in the soft and hard energy bands, respectively. Each sinusoidal component has a period of 72.14 days, possibly resulting from the ISS orbital precession. All background contributions were estimated from MJD 57,000 to MJD 57,999. For the 2–4 keV light curve, we added a systematic uncertainty of 10%, obtained through the same image fit analysis of the Crab Nebula. Some data points were unusable due to image fit results affected by flux variations of the nearby source 4U 1624–490. Figure 1 shows the count rate evolution of J1621 in all three energy ranges (hard, soft, and total).

2.2. The Neil Gehrels Swift Observatory/X-Ray Telescope (Swift/XRT)

Swift/XRT (Burrows et al. 2005) was used in photon counting (PC) and window timing (WT) modes. For our spectral analysis we corrected for pileup in the PC mode by pairing annular extraction regions around the source with ancillary response files.²⁵ No WT-mode count rates exceeded the 100 counts s^{-1} threshold for pileup (Romano et al. 2006).

The Swift observations provide sporadic coverage of the J1621 outburst. They are distributed in three intervals: the very beginning of the outburst (2017 October), 2018 mid-January to mid-February, and 2018 March to June. We flag Obs. 2, 11, and 35 in Table 1 as unusable for scientific analysis. In obs. 2 we were not able to extract photons in an annulus of sufficient width for a spectral analysis or flux estimation, due to the source’s off-axis location ($\sim 11^{\circ}.3$), the short exposure time (0.1 ks), and the significant pileup (~ 3.7 counts s^{-1}). Obs. 11 was not used as it was on the edge of the 1D field of view, and Obs. 35 was not used due to a short exposure time of 42 s.

To fit the Swift/XRT PC-mode data, we extracted a centroided, circular source region of radius = 20 pixels $\sim 50''$ and a circular background source region, at a similar off-axis angle, with radius of at least $50''$, depending on the actual source position within the field of view. We then extracted spectra and light curves with `xselect` for source and background, created an exposure map, and created ancillary response files for source and background. Using `grppha` we grouped the spectra at a minimum of 10–30 photons per bin, depending on the total source photon count.

To fit the Swift/XRT WT-mode data, we carried out a similar process, using a centroided, rectangular source region of length 20 pixels $\sim 50''$ and a rectangular background region with length of at least $50''$, depending on the source distance from the central pixel of the 1D projection. We used the same methods as for the PC-mode data to extract and prepare the spectra for fitting.

2.3. The Nuclear Spectroscopic Telescope ARray (NuSTAR)

We observed J1621 with NuSTAR (Harrison et al. 2013) three times for a total exposure of ~ 90 ks. NuSTAR consists of two coaligned, grazing-incidence Wolter-I Focal Plane Modules (FPMA/B). Here we flag NuSTAR obs. 15 and 16, which were carried out in data mode 06, while J1621 was 28° from the Sun. In this mode, positional information is only accurate to $2'$, instead of the nominal $8''$. Each observation was divided into Good Time Intervals (GTIs), where the aspect solution was determined by different combinations of Camera Header Units (CHUs).²⁶

We extracted the data for NuSTAR Obs. 15 and 16 by first splitting the cleaned Level 2 event file using the NUSPLITSC command, which produced one event file for each CHU combination (CHUs 2, 3, 1 + 2, 1 + 3, and 2 + 3 were used). For each event file, we created with DS9 circular source regions centered on J1621 with radius = $120''$. This process allowed for visually smooth transitions between CHU switches in the source persistent emission light curve and usually allows for an $\sim 85\%$ enclosed energy fraction (An et al. 2014). It is expected that the data mode 06 encloses a lower percentage of the overall point-source energy. A background region file of the same shape and size was created near the source. We then ran the standard NUPRODUCTS command from HEASOFT V6.22 on each event file to extract light curves and spectra. Spectral fits to NuSTAR data were limited due to high background above 25 keV during our observations.

To extract the spectra in the first NuSTAR epoch (Obs. 12, Table 1) we created a circular source region centered on the NuSTAR centroid with radius $r = 120''$. A background region of the same size and shape was constructed. A response matrix and ancillary response file were created for each spectrum using the NUPRODUCTS routine in HEASOFT. For the other two NuSTAR epochs (Obs. 15 and 16, Table 1), which were taken in mode 06, we extracted spectra separately for each of the five CHU combinations for both focal plane modules A and B. All 10 were fit together, totaling 20 spectra. To avoid mixing the spectra, an ancillary response file and response matrix file were generated for each spectrum individually. Spectrum extraction was done with the same source and background shapes and sizes, but the source centers were chosen to be the NuSTAR data mode 06 source centroid for each combination of CHUs.

2.4. The Neutron Star Interior Composition Explorer (NICER)

Also mounted on the ISS, NICER (Gendreau et al. 2016) comprises 56 coaligned X-ray concentrator optics, each paired with a single pixel silicon drift detector sensitive in the 0.2–12 keV passband (Prigozhin et al. 2012). We started observing J1621 on 2017 October 21, however, due to limited source visibility, only about 700 s of exposure could be collected at that time. Additional observations were collected in

²⁵ See the Swift Leicester Site for details (<http://www.swift.ac.uk/analysis/xt/arfs.php>).

²⁶ See Section 6.7 at https://heasarc.gsfc.nasa.gov/docs/nustar/analysis/nustar_swguide.pdf.

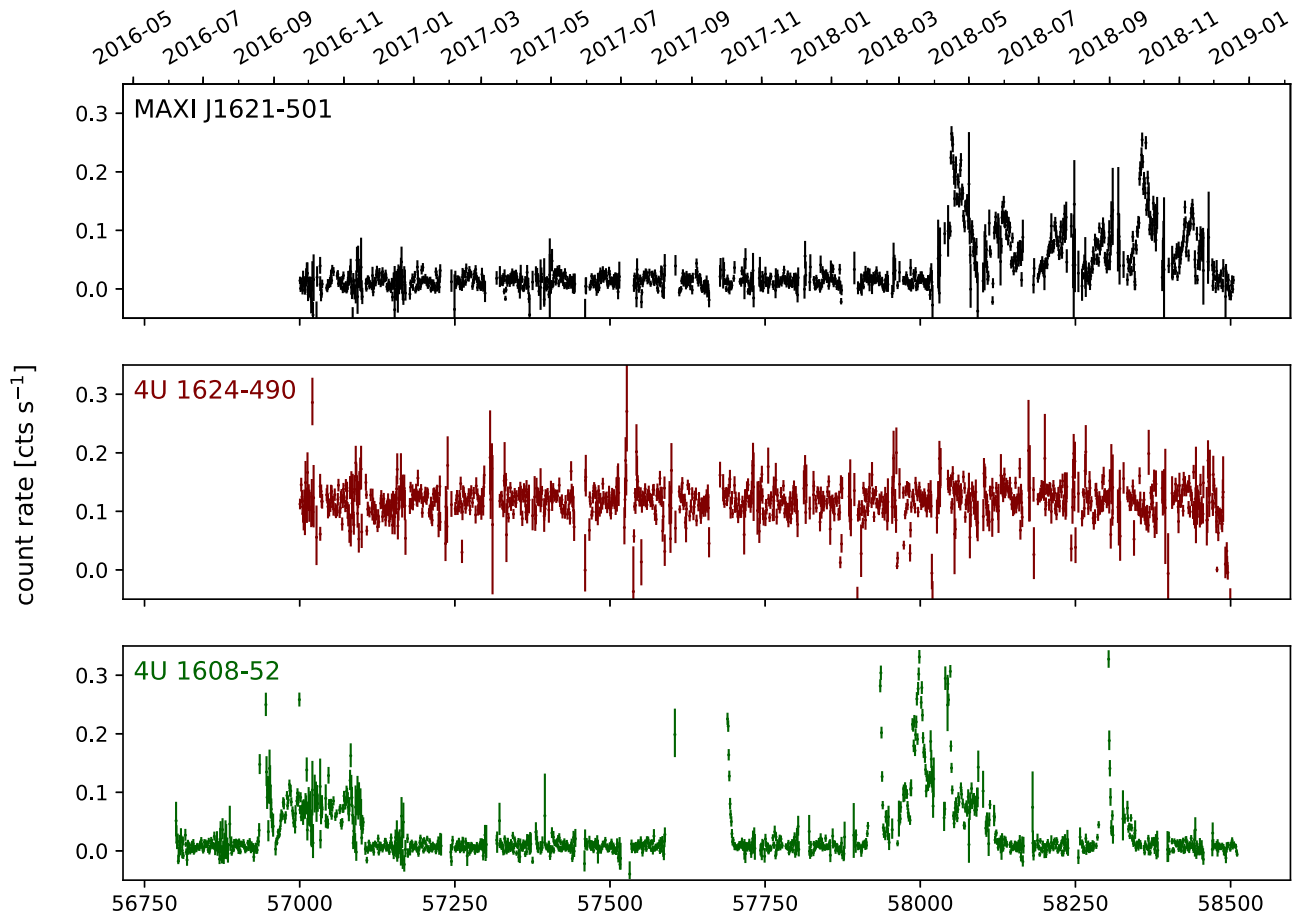


Figure 2. MAXI light curves of two sources in the vicinity of J1621 do not display the ~ 78 day modulation observed in the light curve of J1621. Top to bottom: J1621, 4U 1624-490 (89' away), and 4U 1608-52 (161' away).

2018 February, March, and June. The *NICER* data are available under ObsID 10206301 nn and 10341701 mm , where nn is either 01 or 02, and mm ranges from 01 through 12. Together these data yield roughly 40 ks of unfiltered exposure.

We processed the *NICER* data using the NICERDAS version V004 within HEASOFT 6.24. Four epochs were defined (see Table 1) in which the source did not display rapid changes spectroscopically: epoch 1 is Obs. 6 and 9; epoch 2 is Obs. 26 and 27; epoch 3 is Obs. 29–35; and epoch 4 is Obs. 45–47. The data were filtered using standard cleaning criteria, i.e., a pointing offset $< 54''$ from the *Swift*/XRT enhanced position, $> 30^\circ$ from the dark Earth limb, $> 40^\circ$ away from the bright Earth limb, and outside of the South Atlantic Anomaly. Additionally, we filtered out epochs of enhanced background, determined from the 12–15 keV light curve (see Bult et al. 2018a, 2018b, for details). After filtering, we retained 26.7 ks of good time exposure. The 1–10 keV background contribution to our observations was 0.6–1.5 counts s^{-1} , as estimated from *NICER* observations of blank field regions. For comparison, the source rate in this band varied between ~ 50 –100 counts s^{-1} .

2.5. The Chandra X-Ray Observatory (Chandra)

We observed J1621 for 2.6 ks with the *Chandra*/High-Resolution Camera (Murray et al. 2000, HRC) for best imaging resolution ($\sim 0''.4$) and to avoid pileup. We used `ciao` v4.9.3 `repro` and `dmstat` commands to centroid the source with a 20 pixel radius.

2.6. The INTERNATIONAL Gamma-Ray Astrophysics Laboratory (INTEGRAL)

During its outburst, J1621 was visible within the field of view of the *INTEGRAL* IBIS/ISGRI (Lebrun et al. 2003; Ubertini et al. 2003) and the two JEM-X units (Lund et al. 2003) from 2018 January 27 at 14:29 to 2018 April 11 at 11:00 (UT). Relevant publicly available data were collected during the satellite revolutions 1913–1919, 1922, 1926–1929, 1935, and 1937–1940. We analyzed all data by using version 10.2 of the OFF-LINE SCIENTIFIC ANALYSIS SOFTWARE (OSA) distributed by the ISDC (Courvoisier et al. 2003). *INTEGRAL* observations are divided into “science windows” (SCWs), i.e., pointings with typical durations of ~ 2 –3 ks. Only SCWs in which the source was located to within an off-axis angle of 4° from the center of the JEM-X field of view were included in the analysis. For IBIS/ISGRI, we retained all SCWs where the source was within an off-axis angle of 12° from the center of the instrument field of view.

2.7. The Neil Gehrels Swift Observatory/Ultra Violet Optical Telescope (Swift/UVOT)

We utilized the *Swift*/UVOT (Romig et al. 2004) UVW1, UVW2, and UVM2 filters, with central wavelengths of 2600, 1928, and 2246 Å, respectively. Obs. 2, 3, and 4 were not utilized as J1621 was off the chip.

For each observation, we created a circular source region ($r = 5''$) centered at the best *Chandra* location (Section 3.1) and

Table 2
The Parameters for the Best Fits to the Absorbed PL and Absorbed Disk BB Models

<i>Swift</i> OBSID	Power Law Γ	Disk BB kT keV	UVOT Filter	UVOT 3σ Upper Limit $10^{-17} \text{erg s}^{-1} \text{cm}^{-2} \text{\AA}^{-1}$
00036140001	UVW1	3.49
00042867001	UVM2	4.84
00087355001	UVW1	1.13
00010352001	$1.24^{+0.20}_{-0.20}$	$5.99^{+46.88}_{-2.40}$
00010357001	$1.67^{+0.18}_{-0.18}$	$2.86^{+0.73}_{-0.46}$
00036140002	$1.24^{+0.06}_{-0.06}$	$5.29^{+0.93}_{-0.64}$	UVM2	4.62
00036140003	$1.63^{+0.08}_{-0.08}$	$3.08^{+0.31}_{-0.25}$
00036140004	UVM2	4.23
00087355002	$2.28^{+0.09}_{-0.09}$	$1.85^{+0.11}_{-0.10}$	UVW1	5.83
00036140006	$2.05^{+0.07}_{-0.07}$	$2.09^{+0.10}_{-0.09}$	UVW1	4.54
00036140007	$2.05^{+0.07}_{-0.07}$	$2.13^{+0.10}_{-0.09}$	UVM2	4.42
00036140008	$2.06^{+0.07}_{-0.07}$	$2.09^{+0.10}_{-0.09}$	UVW2	4.57
00036140009	$1.49^{+0.11}_{-0.11}$	$3.57^{+0.59}_{-0.42}$
00036140011	$1.90^{+0.14}_{-0.14}$	$2.47^{+0.33}_{-0.25}$	UVW2	4.55
00036140012	$2.39^{+0.07}_{-0.07}$	$1.69^{+0.07}_{-0.06}$	UVW1	4.57
00036140014	$2.07^{+0.09}_{-0.09}$	$2.10^{+0.14}_{-0.12}$	UVM2	5.49
00036140016	$2.20^{+0.09}_{-0.09}$	$1.92^{+0.12}_{-0.11}$	UVW2	4.33
00036140017	$1.91^{+0.16}_{-0.16}$	$2.35^{+0.35}_{-0.27}$	UVW2	4.82
00036140018	$2.04^{+0.14}_{-0.14}$	$2.12^{+0.24}_{-0.19}$	UVW1	3.63
00010670001	$2.06^{+0.05}_{-0.05}$	$2.12^{+0.07}_{-0.06}$	UVW2	7.31
00010670002	$2.33^{+0.13}_{-0.13}$	$1.82^{+0.16}_{-0.13}$	UVW1	3.36
00010670003	$2.64^{+0.18}_{-0.18}$	$1.50^{+0.15}_{-0.12}$	UVW2	4.55
00010670004	$2.26^{+0.09}_{-0.09}$	$1.84^{+0.10}_{-0.09}$	UVW1	5.16
00010670005	$2.21^{+0.14}_{-0.14}$	$1.95^{+0.20}_{-0.16}$	UVW1	3.88
00010670006	$2.34^{+0.18}_{-0.18}$	$1.89^{+0.24}_{-0.19}$	UVW2	4.69
00010670007	$2.10^{+0.20}_{-0.20}$	$2.06^{+0.35}_{-0.26}$	UVW2	4.57
00010670008	$2.25^{+0.21}_{-0.21}$	$2.04^{+0.36}_{-0.26}$	UVW1	3.28
00010670010	$1.87^{+0.14}_{-0.14}$	$2.62^{+0.37}_{-0.28}$	UVW1	3.81
00010670011	$1.64^{+0.37}_{-0.37}$	$3.04^{+2.80}_{-0.88}$	UVW2	9.35
N_{H} [10^{22} cm^{-2}]	$5.53^{+0.10}_{-0.10}$	$4.22^{+0.07}_{-0.06}$		
red χ^2	3170/2264 = 1.40	3056/2264 = 1.35		

Note. N_{H} was linked between all observations. The UVOT 3σ upper limits are reported in the rightmost column, uncorrected for extinction.

a circular background region ($r = 18''$) near the source. We first retrieved and applied the aspect correction from the USNOB1 catalog using the UVOTSKYCORR FTOOL. We then summed separate exposures with UVOTIMSUM and used UVOTSOURCE to estimate source brightness at the 3σ threshold. The source was not detected in any observations due to the heavy extinction in the Plane. The estimated 3σ upper limits are listed in the rightmost column of Table 2.

2.8. The Gemini Observatory (Gemini)

We utilized the J , H , and K_s filters on the FLAMINGOS-2 instrument (Eikenberry et al. 2004), mounted on Gemini South. Using the *Chandra* localization, we were able to identify an IR counterpart to J1621. The source photometric variation and spectra are reported in A. Bahramian et al. (in preparation).

2.9. The InfraRed Survey Facility (IRSF)

IRSF is a 1.4 m telescope at the Sutherland Observatory, South Africa. We used the simultaneous-imaging camera SIRIUS (Nagashima et al. 1999; Nagayama et al. 2003) on IRSF (Glass & Nagata 2000), which has a 7.7 square arcminute

field of view. We measured magnitudes of 2MASS (Skrutskie et al. 2006) sources in the field of view for a calibrated search for a J1621 counterpart in the J ($1.25 \mu\text{m}$), H ($1.63 \mu\text{m}$), and K_s ($2.14 \mu\text{m}$) bands. Seeing during the 250 s ($10 \text{ s} \times 25$ frames) observations was limited to ~ 2.5 arcsec, determined in the J band. The source was not detected in any of the observations (see Table 3).

2.10. The Australia Telescope Compact Array (ATCA)

We observed J1621 with ATCA (Wilson et al. 2011) on 2017 November 18 between 19:00 UT and 24:00 UT, under project code CX399. We observed at central frequencies of 5.5 GHz and 9 GHz, each with 2 GHz of bandwidth in the 1.5C configuration. The flux and bandpass calibrator was PKS B1934–638. The complex gain calibrator was IERS B1600–489. The data were calibrated with the Multichannel Image Reconstruction, Image Analysis, and Display (MIRIAD, Sault et al. 1995) software package using the standard routines (Sault et al. 1995). We created Stokes I images using the MFCLEAN procedure to properly account for the large fractional bandwidth at these relatively low central frequencies. J1621 was not detected in either band. The flux density at the target

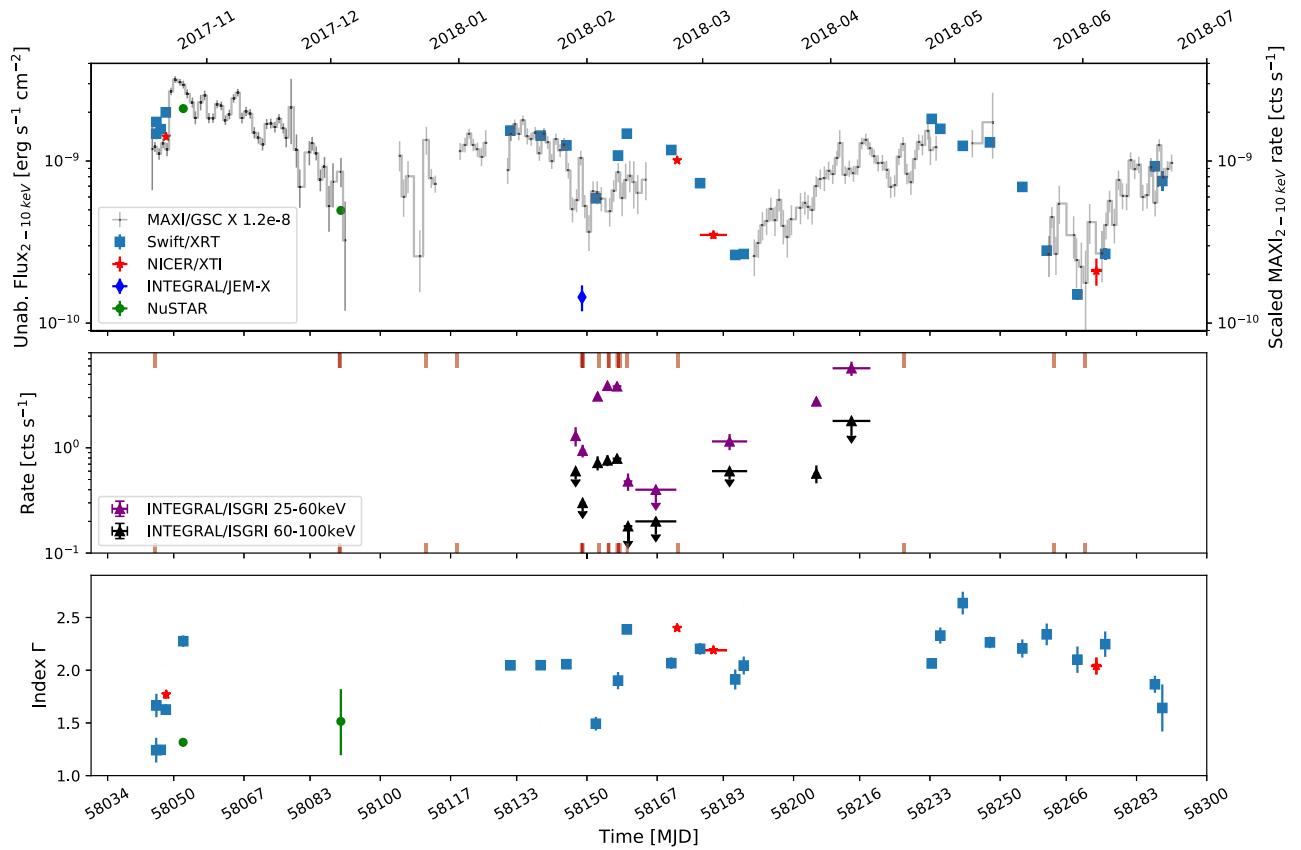


Figure 3. Top: multi-instrument unabsorbed flux evolution of J1621 in the energy range of 2–10 keV. The MAXI count rate data are scaled by an arbitrary factor of 1.2×10^{-8} . The *INTEGRAL*/JEM-X flux point was reported in the energy range 3–10 keV (Lepingwell et al. 2018). Middle: high-energy *INTEGRAL*/ISGRI data in two energy bands, red lines denote the 21 type I X-ray bursts within this interval. Bottom: evolution of the power-law spectral index. Colors follow the legend in the top panel.

location was 2.9×10^{-5} Jy beam $^{-1}$ at 5.5 GHz and 2.2×10^{-5} Jy beam $^{-1}$ at 9 GHz. The off-source rms was 2.4×10^{-5} Jy beam $^{-1}$ at 5.5 GHz and 1.4×10^{-5} Jy beam $^{-1}$ at 9 GHz. To calculate the upper limit of the radio flux density, we took the measured Stokes I flux density at the target location and added it to $3 \times$ the off-source rms. The resulting upper limit values were <0.10 mJy at 5.5 GHz and <0.064 mJy at 9 GHz. A bright, extended source approximately $27'$ to the east of J1621 dominated the field at 5.5 GHz and contributed to the rms in the image, making it significantly higher than the theoretical thermal noise.

3. Persistent X-Ray emission

We discuss below the source localization, its persistent emission light curve and spectral evolution, and the results of our temporal analysis. Throughout our analyses, uncertainties are reported at the 90% level unless otherwise specified.

3.1. X-Ray Source Localization

We triggered our *Chandra* ToO and observed the *Swift*/XRT enhanced error box of the source (Goad et al. 2007; Evans et al. 2009; Bahramian et al. 2017) on 2018 February 22 for 2.6 ks with *Chandra*/HRC-I. The source was seen with a net count rate of 1.77 ± 0.03 counts s $^{-1}$ (signal-to-noise ratio (S/N) > 55 using *celldetect*) at the aimpoint. We determined the

position of J1621 to be at R.A., decl. (J2000) = $16^{\text{h}} 20^{\text{m}} 22^{\text{s}}.09$, $-50^{\circ} 01' 09''.39 \pm 0''.8$; the total location uncertainty is dominated by the *Chandra* systematic pointing error. This is the best-known localization of the source to date.

3.2. X-Ray Light Curve

Prior to the discovery of J1621, this field of the sky had only been observed four times with current X-ray instruments. A 4.6 ks archival *Swift*/XRT observation on 2007 February 6 (OBSID 00036140001) yielded a 3σ upper limit of 1.3×10^{-12} erg s $^{-1}$ cm $^{-2}$ in the 0.3–10 keV range. A *Chandra*/ACIS-S observation on 2008 May 28 for 1.6 ks (OBSID 09602) was also a nondetection with a 90% confidence upper limit of 7.5×10^{-14} erg s $^{-1}$ cm $^{-2}$. The most recent archival data were obtained with *Swift*/XRT (0.3–10 keV) on 2012 June 1 (OBSID 00042867001) and 2017 May 5 (OBSID 00087355001), which also yielded 3σ upper limits of 8.4×10^{-12} erg s $^{-1}$ cm $^{-2}$ and 1.3×10^{-12} erg s $^{-1}$ cm $^{-2}$, respectively. The latter was obtained within the scope of our DGPS program.

Following the source discovery, MAXI observed J1621 continuously from 2017 October 19 until 2019 mid-February on a daily basis (excluding gaps due to Earth occultation and SAA passages). Figure 1 demonstrates the source flux variability, which appears to be episodic. Thus far we have identified six recurring episodes of activity, the primary peaks of which are separated by a ~ 78 day interval, calculated by

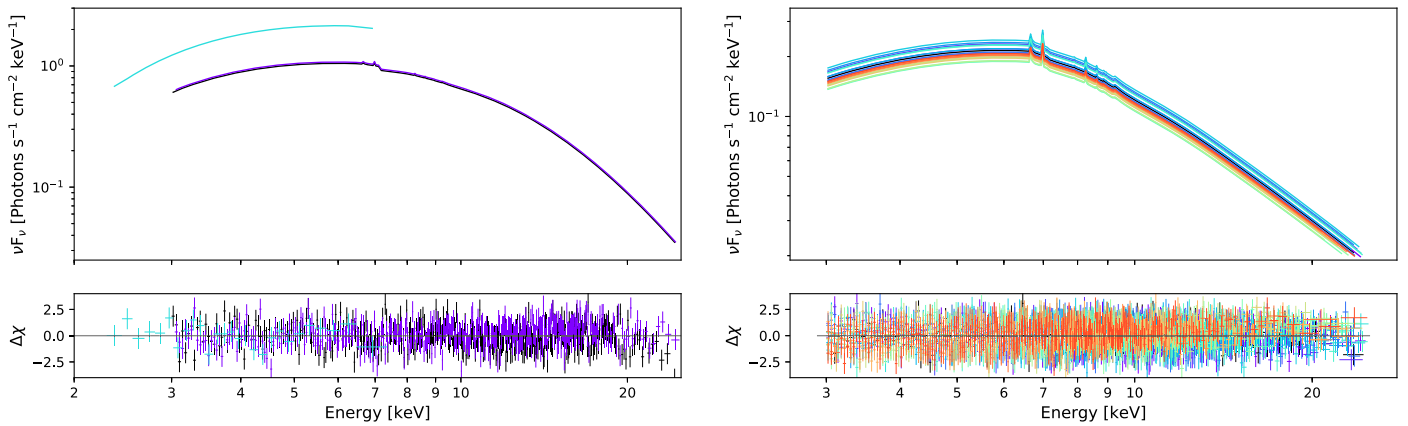


Figure 4. Left: *NuSTAR* and *Swift*/XRT (set 1) persistent emission spectra fit with an absorbed blackbody plus disk reflection model with a multiplicative constant. Only the model is shown. The bottom box shows the fit residuals in units of χ . Right: similar for the remaining *NuSTAR* observations (set 2).

taking the arithmetic mean of the intervals between local maxima in Figure 1. Although this is an intriguing feature, we noted its vicinity to the ISS precession period, so we took several steps to investigate its nature. The field on which J1621 lies contains two other sources, which became active during the outburst of J1621. These sources are 4U 1624–490, an NS LMXB 90' away (Christian & Swank 1997), and 4U 1608–52, an NS LMXB 160' away (Güver et al. 2010). We searched their light curves for similar modulations, assuming that if the J1621 modulation is of instrumental nature and possibly associated with the ISS precession period, the same modulation will appear in their light curves. We plotted the image fit data for all three sources (Figure 2); this method accounts for the contributions of the two nearby sources to the count rate of J1621. Although a significant modulation appears in the data of J1621, the other sources do not exhibit evidence for such an episodic activity. Barring unknown additional instrumental effects due to the ISS, we discuss in Section 5 whether the J1621 episodes are intrinsic source properties.

One additional feature in the light curve is the appearance of the fourth episode at the same intensity as the first one; at the same time, the fifth episode exhibits a structure similar to that of the second. These similarities may indicate a possible secondary period of order 304 days; this claim, however, needs to be substantiated with longer observational intervals during a new source activation.

Figure 3 combines the MAXI data with sporadic observations with *Swift*/XRT, *NICER*/XTI, *NuSTAR*, and *INTEGRAL*/JEM-X and ISGRI. We note here that the MAXI data are in count rates and were scaled along the vertical axis to match the other instruments' observations, which are in flux units. Overall, there is good agreement across all instruments, corroborating that the super-orbital modulations in the light curve are not instrumental in origin. We note that the two *INTEGRAL*/ISGRI light curves are also count rates in two energy bands (25–60 keV, 60–100 keV) with their detection significance measured from the instrument mosaics extracted in different revolutions. The importance of this data set is that it follows the J1621 light-curve rise in the X-ray (top panel) near MJD 58,150. After this rise, the hard X-ray intensity drops rapidly near a peak of soft X-ray emission. The possible nature of this major dip is further discussed in Section 5.

Table 3
IRSF Upper Limits of J1621 Counterparts

Obs.	Instrument/band	3σ lower lim. Vega Mag.
10.	SIRIUS/J	>18.6
10.	SIRIUS/H	>18.0
10.	SIRIUS/ K_S	>17.1

Note. Obs. column is cross-referenced from Table 1.

3.3. X-Ray Spectroscopy

Spectra of LMXBs are usually fit with a thermal component and a nonthermal component. In addition, the spectrum can contain a disk reflection component from ionized species in the accretion disk and Comptonization, produced by upscattering of the incident emission on a free-electron halo. We discuss below our spectral fits to the data. Starting with *NuSTAR* and *NICER*, we determined the continuum and narrow spectral features of J1621. The former mission has a high broadband sensitivity, and the latter has large effective collecting area and high spectral resolution. These fits agree well with *Swift*/XRT observations, in spite of differences in spectral range and resolution. Finally, we show the contribution of *INTEGRAL* at energies up to ~ 200 keV. To model contributions from the interstellar medium we used abundances from Wilms et al. (2000) and cross sections from Verner et al. (1996) in `xspec v12.10.0`.

3.3.1. NuSTAR and NICER

Since the first *NuSTAR* observation (Obs. 12 from Table 1) was contemporaneous with an XRT observation (Obs. 13 from Table 1), they were fitted together to span a larger energy range and to better constrain N_{H} . We designate these two observations as set 1 (*NuSTAR* and *Swift*/XRT). The other two *NuSTAR* observations, which were taken one day apart, were first fitted separately, and the fit parameters were found to be consistent with each other. We, therefore, fitted them jointly to better constrain the spectral model parameters; these two observations (Obs. 15 and 16 from Table 1) we designate as set 2 (only *NuSTAR*). To fit set 1 and set 2, we used a calibration factor between each spectrum with the *NuSTAR* FPMA spectrum and the *NuSTAR* FPMA CHU 2 spectrum used as a reference (i.e., prefactor=1), respectively. The calibration

Table 4

Fits to J1621 Persistent Emission: (*top*) Absorbed Cutoff Power Law Plus Blackbody Plus Lorentzian Emission Line, (*middle*) Absorbed Xillver and Blackbody, (*bottom*) Absorbed Blackbody with Compton Scattering from a Halo of Free Electrons

Set of Spectra	Set 1 (Obs. 12 and 13)	Set 2 (Obs. 15 and 16)
nH (E22 cm ⁻²)	4.23 ^{+0.30} _{-0.29}	3.02 ^{+0.89} _{-0.97}
Γ	0.69 ^{+0.42} _{-0.34}	1.75 ^{+0.38} _{-0.34}
Ecut [keV]	2.77 ^{+0.53} _{-0.64}	5.78 ^{+2.62} _{-2.22}
CPLnorm	0.75 ^{+0.13} _{-0.11}	0.27 ^{+0.12} _{-0.10}
BB kT [keV]	2.32 ^{+0.08} _{-0.09}	1.24 ^{+0.13} _{-0.20}
BB norm	1.70 ^{+1.49} _{-0.83}	3.75 ^{+2.05} _{-1.60}
LineE [keV]	6.31 ^{+0.14} _{-0.14}	6.19 ^{+0.20} _{-0.18}
Width [keV]	3.15 ^{+0.34} _{-0.45}	4.47 ^{+0.40} _{-0.73}
Lnorm (E-3)	8.72 ^{+2.47} _{-2.54}	7.76 ^{+2.62} _{-3.03}
χ ²	1051 with 877 bins (866 dof)	4865 with 4789 bins (4761 dof)
nH (E22 cm ⁻²)	4.39 ^{+0.24} _{-0.14}	1.28 ^{+0.49} _{-0.35}
Γ	1.40 ^{+0.05} _{-0.03}	1.51 ^{+0.32} _{-0.32}
Afe	0.50 ^{+0.17} _{-0.50}	2.49 ^{+2.56} _{-1.35}
Ecut [keV]	5.00 ^{+0.04} _{-5.00}	7.94 ^{+2.03} _{-0.69}
logxi	4.05 ^{+0.06} _{-0.02}	4.07 ^{+0.30} _{-0.18}
norm (E-3)	2.84 ^{+0.20} _{-0.18}	0.44 ^{+0.17} _{-0.12}
BB kT [keV]	1.79 ^{+0.03} _{-0.03}	1.53 ^{+0.03} _{-0.06}
norm	6.99 ^{+0.39} _{-0.42}	3.61 ^{+0.77} _{-0.43}
χ ²	940 with 807 bins (797 dof)	4852 with 4789 bins (4762 dof)
nH (E22 cm ⁻²)	3.65 ^{+0.39} _{-0.39}	0.62 ^{+0.65} _{-0.62}
T ₀ [keV]	0.37 ^{+0.05} _{-0.07}	0.36 ^{+0.06} _{-0.26}
kT _e [keV]	2.51 ^{+0.06} _{-0.05}	4.25 ^{+0.51} _{-0.35}
Tau _p	13.12 ^{+0.84} _{-0.79}	9.00 ^{+1.50} _{-1.28}
Compt norm (E-2)	36.44 ^{+9.50} _{-6.13}	2.37 ^{+1.07} _{-0.63}
BB kT [keV]	1.33 ^{+0.04} _{-0.04}	1.41 ^{+0.02} _{-0.02}
BB norm	26.63 ^{+4.90} _{-4.27}	7.49 ^{+0.73} _{-0.69}
χ ²	962 with 807 bins (798 dof)	5002 with 4789 bins (4763 dof)

Note. Left column is set 1 and the right column is set 2, as described in the text.

factor was left free to vary in the other spectra. The value of the parameter had a maximum difference in set 1 of 12.7% in the FPMA CHU 12 spectrum (average of 6.7%) and a maximum difference in set 2 of 104.1%, in the XRT spectrum, reflecting the calibration difference between *NuSTAR* and *Swift*.

Both sets of spectra (set 1, 2–25 keV, and set 2, 3–25 keV) were independently fitted with an absorbed blackbody (BB) plus a Comptonized emission component (Titarchuk 1994). In set 1, the fit left a systematic residual pattern in the range of 6–7 keV, indicative of the presence of emission features. We then fitted this set with an absorbed BB plus a cutoff power law (PL) model, which resulted in even larger χ² for sets 1 and 2 (see Table 4). This fit still left high systematic residuals at the same energy. Finally, we fitted a disk reflection model, *xillver* (García et al. 2014),²⁷ paired with a BB (Figure 4), which left no systematic residuals. The latter fit decreased the

χ² fit statistic by 22 (χ² = 940) and 150 (χ² = 4852) from the Comptonized BB model for set 1 and set 2, respectively. Three parameters in the *xillver* model were frozen: redshift $z = 0.0$, inclination angle $\text{Incl} = 30^\circ$, and the reflected fraction $\text{refl_frac} = 1.0$ (100% of intensity emitted toward the disk). The quality of data did not allow for good constraints on the inclination angle. Figure 4 shows the fits of both sets to the disk reflection plus BB model and their residuals; the fit parameters are shown in Table 4.

We simulated the *xillver* and BB model (see Appendix) and found that we could not reliably return the best-fit parameters given the quality of our spectra. Along with setting the inclination angle, this informs us that this model cannot be adequately tested, so we restricted ourselves from then on to an absorbed cutoff PL plus BB plus a Lorentzian to model the contribution from a feature near 6.4 keV. This model resulted in reduced χ² = 1.21 in set 1 and reduced χ² = 1.02 in set 2; it also allowed us to estimate the line continuum equivalent widths (0.27 keV and 1.43 keV, respectively) and fluxes (9.13×10^{-11} erg s⁻¹ cm² and 6.30×10^{-11} erg s⁻¹ cm², respectively). The fit parameters are recorded in Table 4.

We split the *NICER* data into four distinct epochs (plotted as red stars in Figure 3), where each epoch represents a closely spaced set of observations (see Section 2.4). For each epoch we extracted the 1–10 keV spectrum and fit it with several absorbed (*Tbabs*) models. We tried PL, disk blackbody (DBB), BB with Comptonization, and BB with a cutoff PL. Of these models, the PL consistently fit the best, with the DBB providing a worse fit (0.1–0.8 units of reduced χ²). The other models did comparably well but with more parameters and were thus discarded from further consideration.

The best-fit PL parameters are shown in Table 5. We note here that of the four PL spectral indices (Γ = 1.77 ± 0.04, 2.40 ± 0.02, 2.19 ± 0.02, and 2.04 ± 0.08), three are above 2 and one is 1.77. The softer spectra seem to all have occurred during episodic minima, while the hardest of the four was measured during the ascending part of the first episode. The reduced χ² values (1.1, 1.3, 1.3, 1.2) mostly reflect systematic residuals around 1.7 and 2.1 keV, both of which are known instrumental features.

3.3.2. *Swift*/XRT

We loaded all XRT spectra (extracted and grouped) using *pyxspect* and fitted them jointly with multiple functions, including BB, disk reflection, and nonthermal models. Of these, the best fits were provided by an absorbed DBB and a single absorbed PL model (Figure 5), with χ² = 3056 and 3170 for 2264 dof, respectively. Unlike with the *NICER* fits, both models fit the *Swift*/XRT data equally well, and we report these results in Table 2. We first fitted all observations keeping all parameters free to vary. The resulting N_{H} values were in the 90% confidence interval range ($4.09_{-0.86}^{+0.97}$ – $6.13_{-0.34}^{+0.35}$) × 10²² cm⁻². We then linked N_{H} between all observations; these fits resulted in N_{H} of $5.53_{-0.10}^{+0.10}$ × 10²² cm⁻² and $4.22_{-0.06}^{+0.07}$ × 10²² cm⁻², for the PL and DBB models, respectively.

The DBB fits the *Swift*/XRT data slightly better, however, we utilized the PL spectral parameters for comparison with those of the *NuSTAR* data. We found that the *Swift*/XRT best-fit spectral indices, Γ, show random variability between 1.24 ± 0.20 and 2.64 ± 0.18 (Figure 3, bottom panel). Three data sets show high, positive residuals below 2 keV. This could be due to the presence of a low-energy, narrow-band

²⁷ *Xillver* is a subset of *relxill*: <http://www.sternwarte.uni-erlangen.de/~dauser/research/relxill/>.

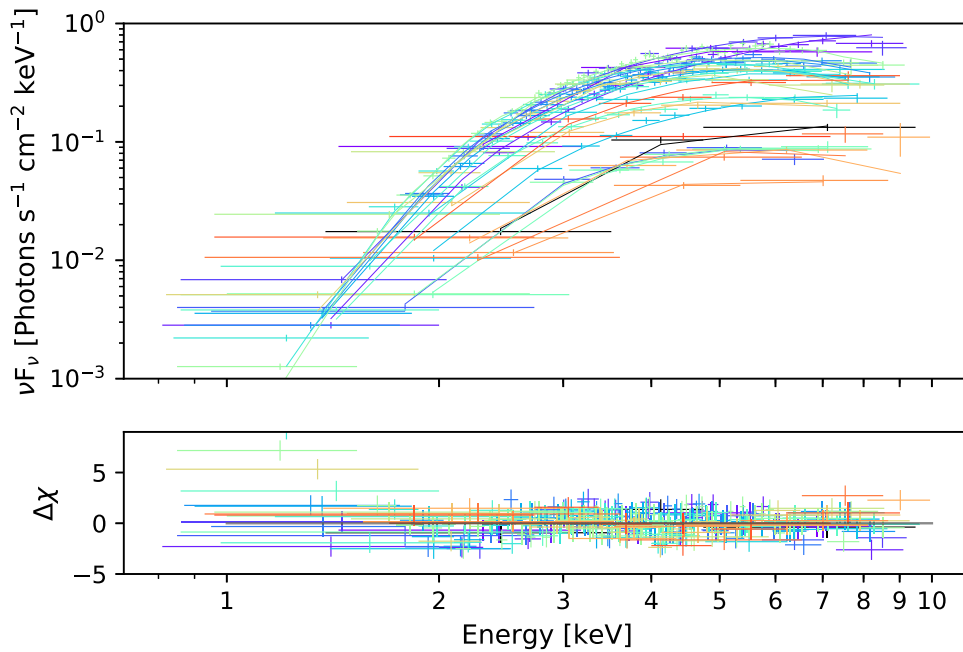


Figure 5. *Swift*/XRT data jointly fitted with an absorbed PL model. Data are binned to a minimum of 15 photons for ease of viewing.

Table 5

The Spectral Parameters Best Fit to Four Epochs of *NICER*/XTI Data

Epoch	nH 10^{22} cm^{-2}	Γ	Flux $_{2-10 \text{ keV}}$ $10^{-9} \frac{\text{erg}}{\text{s cm}^2}$	χ^2/dof	Red. χ^2
1	5.1 ± 0.1	1.77 ± 0.04	1.41 ± 0.02	744/655	1.14
2	5.7 ± 0.1	2.40 ± 0.02	1.01 ± 0.01	911/676	1.35
3	4.8 ± 0.3	2.19 ± 0.02	0.35 ± 0.02	958/717	1.34
4	5.5 ± 0.2	2.04 ± 0.08	0.21 ± 0.04	687/599	1.15

component, which we attempted to fit with a second BB; other LMXB spectra have been successfully fit with multitemperature blackbody models, usually attributed to the accretion disk (the “Eastern Model” of Mitsuda et al. 1989). The result was a lower fit statistic but unconstrained fit parameters, since the component lies near the edge of the spectral band. This BB component was consequently dropped from the model.

3.3.3. INTEGRAL and MAXI

We extracted the *INTEGRAL* IBIS/ISGRI mosaics in the 25–60 keV and 60–100 keV energy bands and inspected the detection significance of the source in these mosaics and the correspondingly measured count rates by IBIS/ISGRI in order to search for possible spectral variations. We show the results of this analysis in Table 6. As no significant variations in the source hardness ratio were measured, we extracted two spectra: the first summed up all data in revolutions 1914–1917 to obtain the best signal-to-noise ratio, and the second used the data in revolution 1935, which is separated by the other revolutions by slightly more than 20 days but is characterized by a relatively high source detection significance. We followed the same strategy for the extraction of the JEM-X1 and JEM-X2 spectra. In all cases, we removed from the data 1 ks of exposure around the 11 type I bursts detected with JEM-X in order not to contaminate the spectrum of the persistent emission.

The combined ISGRI and JEM-X spectra from revolutions 1914–1917 (effective exposure time of 60.8 ks for ISGRI and 4.7 ks for each of the two JEM-X) could be well described ($\chi^2_{\text{red}} = 1.06 = 87/82$) by using a cutoff PL model. We fixed for all fits to the *INTEGRAL* spectral data the value of the absorption column density at $2.5 \times 10^{22} \text{ cm}^{-2}$, as they were not sensitive to variations of this parameter within a factor of a few from this value. We measured in this case a PL photon index of 1.96 ± 0.06 , a cutoff energy of $100^{+40}_{-24} \text{ keV}$, and a 3–100 keV flux of $1.03 \times 10^{-9} \text{ erg s}^{-1} \text{ cm}^{-2}$. The normalization constants introduced to take into account the inter-calibrations between the different *INTEGRAL* instruments were all compatible with unity (within the associated uncertainties). The statistics of the data collected in revolution 1935 (effective exposure time of 60.8 ks for ISGRI and 4.7 ks for each of the two JEM-X) are significantly lower than that in revolution 1914–1917 and thus a simple absorbed PL model can describe these data well ($\chi^2_{\text{red}} = 1.00 = 16/16$). We measured in this case a photon index of 1.3 ± 0.5 . If a cutoff PL model is used for the fit and the cutoff energy is fixed to the above value of 100 keV (resulting in $\chi^2_{\text{red}} = 1.00 = 16/16$), then the photon index of the PL in revolution 1935 would be 1.0 ± 0.5 , i.e., slightly harder than that measured for the revolutions 1914–1917 (we fixed in all cases the absorption column density at $2.5 \times 10^{22} \text{ cm}^{-2}$). We show, as an example, the ISGRI plus JEM-X spectra of the source obtained from the revolutions 1914–1917 data in Figure 6, together with the best-fit model and the residuals from the fit. Although of low significance, we note the presence of large residuals at $\sim 6 \text{ keV}$, in accordance with the results in the *NuSTAR* data.

Finally, we used the MAXI data to obtain the source count rate hardness evolution, defined as the hard band minus the soft band divided by the sum of the bands, during MJD 58,000–58,492 (Figure 1 (bottom)). We excluded time bins with count rates below 0 counts s^{-1} (due to background subtraction) and time bins where the absolute value of the hardness ratio plus error is larger than one. Figure 3 (bottom)

Table 6
Count Rates and Hardness Ratios Obtained from All IBIS/ISGRI Data Collected during the Outburst of J1621

Revolution	Time Span (MJD)	Counts s ⁻¹ (25–60 keV)	Det. Sign. (25–60 keV)	Counts s ⁻¹ (60–100 keV)	Det. sign. (60–100 keV)	Hardness Ratio (σ)
1913	58146.81–58147.72	1.30 ± 0.27	4.8	<0.6
1914	58148.26–58149.65	0.94 ± 0.13	7.0	<0.3
1915	58152.13–58153.04	3.08 ± 0.16	18.9	0.72 ± 0.11	6.4	0.23 ± 0.04
1916	58154.40–58155.53	3.89 ± 0.14	28.8	0.76 ± 0.09	8.2	0.20 ± 0.02
1917	58156.24–58158.34	3.84 ± 0.09	40.9	0.79 ± 0.06	12.3	0.21 ± 0.02
1918	58158.90–58160.99	0.48 ± 0.09	5.7	<0.18
1919–1922	58161.72–58171.63	<0.40	...	<0.20
1926–1929	58180.26–58188.78	1.15 ± 0.20	5.7	<0.6
1935	58204.87–58206.18	2.76 ± 0.17	16.2	0.57 ± 0.11	5.1	0.21 ± 0.11
1937–1940	58209.45–58218.59	5.70 ± 0.88	6.5	<1.8

Note. Values of the count rate preceded by < correspond to 3σ upper limits. For comparison, the count rates of the Crab in the 20–60 keV and 60–100 keV energy bands are 99.4 ± 0.2 counts s⁻¹ and 25.6 ± 0.1 counts s⁻¹, respectively (we used the publicly available observations of the Crab carried out during the satellite revolution 1921 for a total of 45 ks).

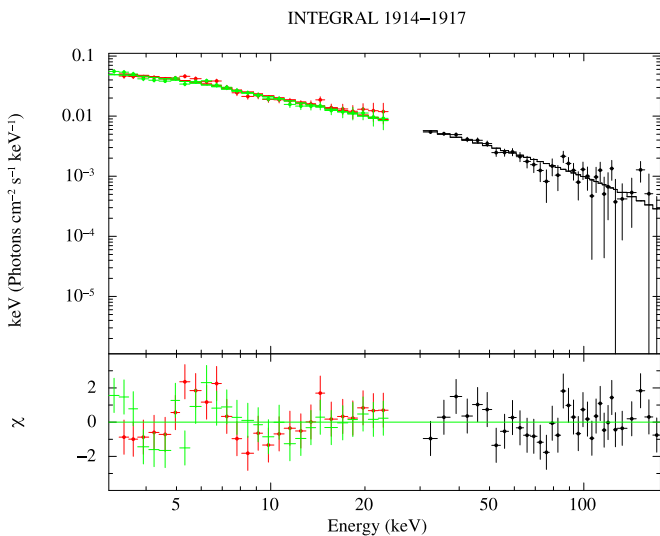


Figure 6. The *INTEGRAL* spectra extracted from the combined data in revolutions 1914–1917. The ISGRI data are in black, the JEM-X1 data in red, and the JEM-X2 data in green. The best-fit model is obtained with a cutoff power law and the residuals from the best fit are reported in the bottom panel of the figure.

shows the PL indices of the spectral fits of the *Swift*/XRT, *NuSTAR*, and *NICER* data points.

3.4. X-Ray Timing

We searched the second *NuSTAR* observation (Obs. 15, Table 1) for QuasiPeriodic Oscillations (QPO) in the source using the STINGRAY timing package (Huppenkothen et al. 2016, 2019) on a light curve spanning 19 ks (3–79 keV). The data were first barycentered in the NUPRODUCTS routine using the operations-provided orbit file and the source centroided coordinates.

We produced an averaged periodogram using segments of 2048 s duration. The final periodogram includes seven individual segments averaged together, utilizing all contiguous GTI intervals longer than the segment length. Because of the source’s brightness, the *NuSTAR* data were strongly affected by dead time (Bachetti et al. 2015). We corrected the periodograms of individual segments using the Fourier Amplitude Differencing

(FAD) technique of Bachetti & Huppenkothen (2018). In short, the FAD method utilizes the light curves of the two different detectors on board *NuSTAR* to compute the difference of the Fourier amplitudes in the two detectors, which can be used to separate intrinsic source variability from the frequency-dependent effects of dead time. After correction, the segments were averaged together to produce a dead time–corrected averaged periodogram (Figure 7).

We used the method laid out in Vaughan (2010) to search for narrow quasiperiodic signals in the averaged periodogram. We modeled the periodogram with a PL plus a constant to account for the white-noise level, using fairly wide, uninformative priors for the parameters (Table 7). We first fitted the model to the data and computed the maximum outlier in the residuals. Subsequently, we used Markov Chain Monte Carlo (MCMC) implemented in the Python package *emcee* (Foreman-Mackey et al. 2013) to sample the parameter space of the models. We then generated simulated periodograms from random samples from the posterior probability distribution. For each, we fitted a power-law model, and computed the highest outlier in the residuals of these simulated periodograms. We then compared the highest outliers derived from the simulated periodograms according to our null hypothesis (no signal) to the highest outlier in the observed periodogram.

There is a potential candidate detection of a narrow quasiperiodic signal at $\nu = 0.0088$ Hz, or a period of $P = 113$ s. However, the trial-corrected significance is only $p = 0.05$, indicating that this signal could potentially be explained by noise. In order to independently confirm the signal, we also searched *Swift* Obs. 13 for a signal at the same frequency and found no trace of a similar QPO in this data set. However, it is important to note that the *Swift* data set was much shorter (566 s total duration) and was heavily affected by pileup, with only a fraction of the photons actually recorded. It is, therefore, possible that the lack of signal in the *Swift* data could be related to the data quality.

4. Type I X-Ray Bursts

Twenty-four type I X-ray bursts were observed from J1621 by four instruments: 11 with MAXI, 11 with *INTEGRAL*, 2 with *NuSTAR*, and 1 with *NICER*. One burst was seen with both *INTEGRAL* and MAXI. This unambiguously identifies J1621 as a system hosting an NS undergoing nuclear burning

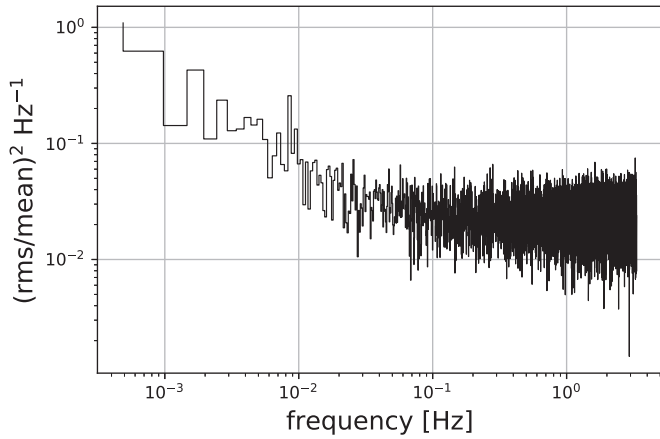


Figure 7. Averaged periodogram of the *NuSTAR* data from 2017 December 2. There is a candidate QPO at $\nu = 0.0088$ Hz, but its significance is low ($p = 0.05$, corrected for 6826 frequency trials).

Table 7

Parameter Definitions and Prior Probability Distributions for the Power Law + Constant Model Used to Fit the Periodogram and Simulate Data Sets from the Null Hypothesis

Parameter	Definition	Prior Probability Distribution
Γ	power-law index	Uniform(0,5)
$\log A_{\text{PL}}$	power-law amplitude	Uniform(-20,20)
$\log A_{\text{noise}}$	Poisson noise amplitude	Uniform(-10,10)

Table 8

A List of the Type I X-Ray Bursts Detected from J1621

Burst	Instrument	Onset Time	Day
		UTC	MJD
1.	MAXI/Cam2	2017 Oct 19 11:36:52	58045.48393
2.	<i>NuSTAR</i> /FPMA+B	2017 Dec 03 01:29:17	58090.06200
3.	<i>NuSTAR</i> /FPMA+B	2017 Dec 03 05:01:02	58090.20905
4.	MAXI/Cam2	2017 Dec 24 03:35:00	58111.14930
5.	MAXI/Cam2	2017 Dec 31 14:13:24	58118.59263
6.	<i>INTEGRAL</i>	2018 Jan 30 15:19:48	58148.63875
7.	MAXI/Cam1+2+7	2018 Jan 30 21:13:00	58148.88402
	<i>INTEGRAL</i>	2018 Jan 30 21:13:02	58148.88405
8.	<i>INTEGRAL</i>	2018 Jan 31 01:39:22	58149.06900
9.	<i>INTEGRAL</i>	2018 Feb 03 21:51:07	58152.91050
10.	<i>INTEGRAL</i>	2018 Feb 06 03:42:09	58155.15427
11.	<i>INTEGRAL</i>	2018 Feb 06 08:01:32	58155.33440
12.	<i>INTEGRAL</i>	2018 Feb 08 06:30:15	58157.27101
13.	<i>INTEGRAL</i>	2018 Feb 08 13:37:40	58157.56782
14.	<i>INTEGRAL</i>	2018 Feb 08 16:40:52	58157.69505
15.	<i>INTEGRAL</i>	2018 Feb 09 01:29:09	58158.06191
16.	<i>INTEGRAL</i>	2018 Feb 10 18:20:47	58159.76443
17.	<i>NICER</i> /XTI	2018 Feb 22 22:34:00	58171.94247
18.	MAXI/Cam1+2+7	2018 Apr 18 19:42:03	58226.82086
19.	MAXI/Cam2	2018 May 24 22:44:23	58262.94748
20.	MAXI/Cam5	2018 Jun 01 11:36:03	58270.48336
21.	MAXI/Cam2	2018 Aug 05 11:36:39	58335.48378
22.	MAXI/Cam5	2018 Aug 12 15:16:16	58342.63629
23.	MAXI/Cam1+2+7	2018 Sep 02 05:02:12	58363.20986
24.	MAXI/Cam2	2018 Oct 16 13:57:02	58407.58127

on the surface. Table 8 exhibits all burst onset times, dates, and the detecting instrument(s).

4.1. Light Curves

We measured the duration of two *NuSTAR* bursts (temporally binned at 1 s) by using the T_{90} method, first developed by Kouveliotou et al. (1993) for gamma-ray burst duration measurements. Burst 2 and 3 (Table 8) durations were found to be 19 ± 2 s, and 24 ± 2 s, respectively. We carried out the same approach with the burst observed with *NICER* and found $T_{90} = 33 \pm 2$ s. We note that these differences in burst duration may come from the spectral range to which each instrument is sensitive: longer durations are expected in softer energy bands for the typical BB spectrum that reaches $kT \sim 2$ keV (Lewin et al. 1993), which is what we observe.

In the *NuSTAR* energy range, we expect a similar burst duration distribution to that of *INTEGRAL*/JEM-X (3–20 keV) (top left panel of Figure 4; Chelovekov et al. 2017). The *NuSTAR* burst durations are longer than most observed with JEM-X, the distribution of which peaks at ~ 10 s. Despite a nonuniform energy range for these comparisons, all three burst durations lie within the range of 10–100 s, where 111/159 $\approx 70\%$ have been recorded (Table 2 of Galloway & Keek 2017).

The MAXI observations totaled ~ 144 ks over 300 days, during which we found 11 significant type I bursts, with an average peak count rate of ~ 2 counts $\text{s}^{-1} \text{cm}^{-2}$ (2–20 keV band).

4.2. Spectroscopy

We fitted the *NuSTAR* burst spectra with two components: an absorbed BB plus disk reflection, frozen at the best-fit parameters of the persistent emission spectrum (see Section 3.3), and a second absorbed BB (BB2). We split each burst into five intervals chosen to cover the rise part of the burst (two bins), its peak, and its decay (two bins). The kT evolution of the BB2 component is shown in Figure 8, left and center panels.

Burst 17 was observed during Obs. 26 with *NICER*. To observe the full burst, we relaxed the bright Earth elevation filter to include those data taken $>35^\circ$ from the limb. To establish the persistent level, we fitted 125 s of preburst emission, which is well described by a PL with $\Gamma = 2.70 \pm 0.10$ and $N_{\text{H}} = (6.1 \pm 0.3) \times 10^{22} \text{ cm}^{-2}$ ($\chi^2/\text{dof} = 216/201 = 1.08$). The persistent flux was at $F_{1-10} = (2.07 \pm 0.16) \times 10^{-9} \text{ erg s}^{-1} \text{ cm}^{-2}$. Freezing these parameters, we added a BB component and carried out a time-resolved approach for six time bins. The result is shown in Table 9 and in the rightmost panel of Figure 8. All three bursts showed a similar kT evolution.

For the brightest *INTEGRAL* burst, we obtained the effective area corrected peak flux of $1.8 \pm 0.3 \text{ counts s}^{-1} \text{ cm}^{-2}$ at 2–10 keV, which corresponds to $F_{\text{bol}} \sim 2.3 \times 10^{-8} \text{ erg s}^{-1} \text{ cm}^{-2}$. Temporally, the burst showed a 10 s monotonic rise followed by an exponential decay ($e^{-\tau/1\text{s}}$, with $\tau = 9 \pm 3$ s). This gave an effective burst duration of $\tau_b = 18$ s.

In order to search for additional bursts observed with *INTEGRAL*, we extracted the JEM-X1 and JEM-X2 light curves with a time resolution of 2 s. A total of 11 bursts were found (see also Chenevez et al. 2018), and we report the onset time of all these events in Table 8. The bursts from the source were relatively faint for JEM-X and we could extract a

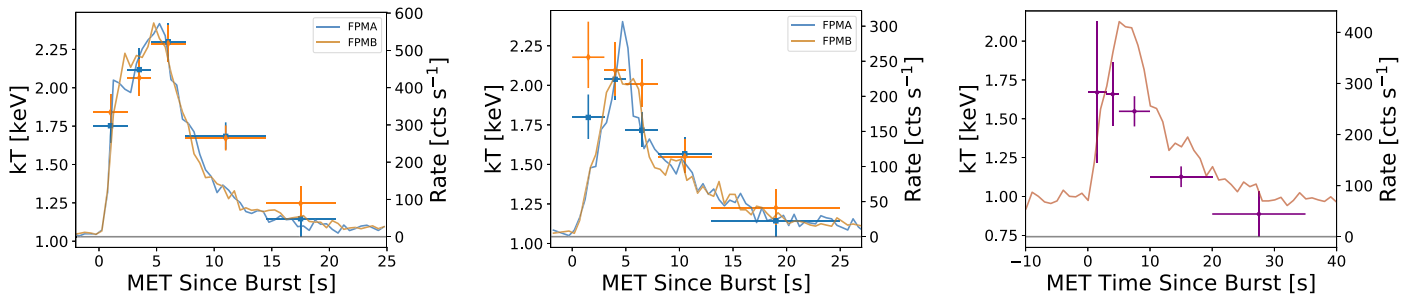


Figure 8. The BB2 kT parameter for burst 2 (left), burst 3 (center), and burst 17 (right). Overplotted are the count rates in 1 s bins, with the corresponding scale on the right side vertical axis.

Table 9

The Spectral Parameters Best Fit to Six Time Bins (Time Since Burst Onset) within the Type I X-Ray Burst Observed with *NICER*/XTI

Bin (s)	N_H (10^{22} cm^{-2})	kT_{BB} (keV)	F_{1-10} (10^{-9})	χ^2/dof	red. χ^2
1.0–3.0	6.1 ± 0.3	$1.40^{+0.34}_{-0.23}$	1.86 ± 0.28	228/218	1.06
3.0–5.0	Linked	$1.45^{+0.19}_{-0.15}$	5.57 ± 0.53	230/224	1.04
5.0–10.0	Linked	1.49 ± 0.09	6.97 ± 0.37	262/261	1.01
10.0–20.0	Linked	1.11 ± 0.06	2.33 ± 0.16	284/260	1.09
20.0–35.0	Linked	0.81 ± 0.07	0.48 ± 0.08	251/243	1.03
35.0–50.0	Linked	...	< 0.50	246/237	1.05

meaningful spectrum during the 8 s around the peak only for the 11th burst, which was also the brightest (reaching about $150 \text{ counts s}^{-1}$ in the 3–20 keV energy band; note that integrations shorter than 8 s are not possible with the standard OSA software). We fitted the JEM-X1 and JEM-X2 spectra with a BB model (the absorption column density was fixed to $2.5 \times 10^{22} \text{ cm}^{-2}$). We used in the fit as a background the spectrum extracted during the remaining available exposure time of the SCW, where the burst was identified (SCW ID. 191800230010). We measured a BB temperature of $kT = 1.9 \pm 0.3 \text{ keV}$, a radius of $13.5 \pm 3.0 \text{ km}$ (assuming a distance of 8.4 kpc), and a 3–20 keV flux of $(3.2 \pm 0.6) \times 10^{-8} \text{ erg s}^{-1} \text{ cm}^2$ (all uncertainties are given at 90% confidence level). We did not find evidence of a clear photospheric radius expansion in any of the JEM-X bursts. Chenevez et al. (2018) mentioned that the burst of 2018 February 3 at 21:51:07 might have undergone a photospheric radius expansion, but we show in Figure 9 that the statistical quality of this event is too low to draw any firm conclusions.

4.3. X-Ray Timing

We searched the burst 17, seen with *NICER*, for burst oscillations. For our search we set up a sliding window of length T and stride $S = T/2$. The number of strides is set such that the last window is at most 35 s after the burst onset. For each window we computed the power spectrum and considered the power spectral bins for frequencies between 50 and 1000 Hz. We then compared the obtained powers with a detection threshold treating all trials (counting every spectral bin, of every window stride) as though they were independent (see, e.g., van der Klis 1989, for a description of power spectrum detection thresholds). We applied this search strategy for $T = 2, 4, \text{ and } 8$, but no burst oscillations were detected.

5. Discussion

J1621 was discovered with MAXI on 2017 October 19 at an X-ray flux approximately four orders of magnitude higher than its deepest upper limit emission in quiescence. It is the first DGPS transient which we followed up with a comprehensive multiwavelength observational campaign to identify its nature. The source was successfully classified as the 111th Type I X-ray burster,²⁸ after it was detected to emit type I X-ray bursts, soon after its outburst (Bult et al. 2018b); in the following 15 months, a total of 22 additional bursts were detected with four separate X-ray instruments.

The source persistent emission spectrum can be adequately described with a three-component model: an absorbed thermal feature (BB), a nonthermal feature (PL), and an emission feature (fit with a Lorentzian centered at $\sim 6.4 \text{ keV}$) indicating an ionized Fe reflection line from an accretion disk. There is clear spectral evolution during the outburst, with the hardest spectra appearing at the rising part of the initial outburst ($\Gamma = 1.4$), while the remaining available spectra cluster around $\Gamma \sim 2$. We note here, however, that we only had good coverage of the light curve at the beginning of the outburst and sporadic *Swift*/XRT data thereafter.

The X-ray light curve of the source appears to be episodic, with at least six distinct peaks separated at ~ 78 days. Simultaneous *Swift*/XRT and *INTEGRAL* observations confirm the episodic nature of the source with one apparent discrepancy: during $\sim \text{MJD } 58,150$ and $58,159$ (see Figure 3), there is a flux rise in the *Swift*/XRT accompanied with a similar rise in the *INTEGRAL* light curve. However, immediately after the peak, the source is not detected with *INTEGRAL*, while it is still well detected with XRT. We attribute this increase of the nonthermal photon intensity to inverse Compton scattering in a

²⁸ See also the web page of Jean In't Zandt: <https://personal.sron.nl/~jeanz/bursterlist.html>.

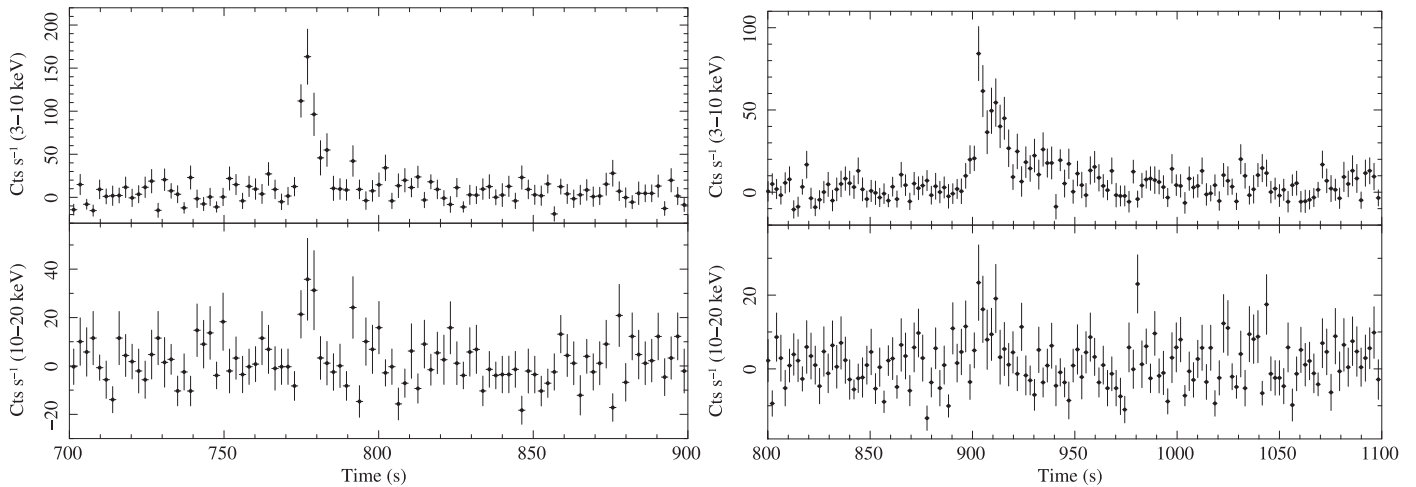


Figure 9. Two examples of bursts observed by JEM-X. We show on the left the 11th burst that achieved the highest peak flux (see the text for details). On the right, we show the burst that was reported to have undergone a photospheric radius expansion but for which we concluded that the statistics are too low to draw a firm conclusion.

hot free-electron halo surrounding the NS. The incident thermal spectrum from the 11 bursts emitted during this interval would have provided a large photon flux, which was subsequently upscattered to the *INTEGRAL*/IBIS energy range on a short timescale due to the impulsive nature of the burst. After the paucity of bursts, the soft X-rays declined slowly, while the hard X-rays disappeared rapidly.

Besides the long-timescale light-curve modulation, a noteworthy characteristic of the two *INTEGRAL* light curves in Figure 3 is the moderate disagreement with that in the low-energy band. This suggests a somewhat different origin for contributions above and below 10 keV. The spectroscopic fitting of the *Swift*/XRT and *NICER* data presents the case that at low energies there is a mix of spectral components below 10 keV. At higher energies, the power-law shape in the *INTEGRAL* spectra (see Figure 6) is much simpler to interpret. It is perhaps suggestive of inverse Compton emission produced by nonthermal relativistic electrons. Alternatively, and probably more appropriate for accreting systems that have moderate-to-high opacities, it resembles the classic unsaturated Comptonization spectrum realized in models of accreting BHs, such as in Cyg X-1 or in active galactic nuclei. The power law arises due to repeated scatterings of lower energy photons by hot, thermal electrons of temperature T_e that slowly increases the photon energy until it is close to kT_e . The power law marks the scale-independence of the Compton upscattering, and its slope depends only on the mean energy gain per collision, $\langle \Delta E \rangle = 4kT_e$ for nonrelativistic electrons, and the probability of loss of photons from the scattering zone.²⁹ The resulting differential photon spectrum is described by

$$\frac{dN}{dE} \propto E^{-\alpha}, \quad \alpha = -\frac{1}{2} + \sqrt{\frac{9}{4} + \frac{4}{y}},$$

$$y = \frac{4kT_e}{m_e c^2} \max\{\tau, \tau^2\}, \quad (1)$$

²⁹ The interested reader may wish to consult Chapter 7 of Rybicki & Lightman (1979) for a summary of its development as a solution of the Kompaneets equation.

with the Compton y parameter normally in the domain $y < 1$. This parameter is the product of the average fractional energy change per scattering and the mean number of Thomson scatterings, and τ is the scattering Thomson optical depth. The index α is a declining function of y . The extension of the power law persists until an exponential turnover arises at $E \sim kT_e$.

If such a coronal Comptonization picture is used to interpret the *INTEGRAL* spectra, then the index provides a measure of the opacity and/or the temperature. The measured value of $\alpha \sim 1.3 \pm 0.5$ during revolutions 1914–1917 suggests a value $y \sim 4$ –5. Temporally, one expects a corona proximate to an accretion disk to be quite variable, perhaps due to magnetic field line flaring activity, much like the solar corona with its mass ejections. The field can be a source for energization of the system. The result is varying or chaotic time profiles. This is consistent with the *INTEGRAL* ISGRI fluxes presented in Figure 3. Flux variations probably trace coronal electron heating rates since the seed photons of disk origin should be approximately constant in luminosity. Enhanced fluxes produced by electron density n_e increases would raise τ , trapping photons more effectively in the Comptonizing cloud and hardening the emergent spectra (lower α). A similar characteristic would be realized by hotter electrons. This degeneracy of information can only be disentangled with the observation of a spectral turnover at different epochs, thereby constraining T_e as a function of time. Unfortunately, the *INTEGRAL* spectra do not clearly exhibit such quasi-exponential turnovers, so that $kT_e \gtrsim 100$ keV is inferred.

Volumetric influences complicate this picture somewhat. It is quite possible that magnetic squeezing of electrons by mobile field lines can adiabatically increase the density and temperature of the hot electrons simultaneously. A noteworthy characteristic of the two *INTEGRAL* light curves in Figure 3 is that the hardness ratio (and therefore α) does not in fact vary much with time. Then the flux variability and implied spectral constancy could be driven by density fluctuations coupled to changes in the effective volume V of the Comptonization zone. With $\tau \propto n_e V^{1/3}$ ($\lesssim 1$), if $n_e \propto V^{-\beta}$, then one infers $T_e \propto V^{\beta-1/3}$ in order to keep the Compton y parameter approximately constant. For plasma flow connected to divergent/convergent coronal field lines, values of $\beta \sim 2/$

3 are expected for wind-like expansions/contractions, indicating that small or modest temperature changes should accompany the observed variability. In particular, volume contractions should induce coupled increases in both density n_e and temperature T_e , with $T_e \propto (n_e)^{1/2}$. This coupling defines a potential diagnostic of the coronal interpretation, though to bring it to fruition requires a more sensitive hard X-ray/soft gamma-ray telescope.

The episodic nature of the observed outbursts is intriguing. A possible explanation for the 78 day variations in its light curve may be the so-called “super-orbital periods” or long periods. These have been noted in a number of low- and high-mass X-ray binaries. A better name for them would be “long timescale modulations,” since very often they are not strictly periodic; individual modulations in the J1621 light curve vary from approximately 50 to 90 days in duration. For quite a few systems there is a broad correlation of this long timescale modulation with orbital period, though with a fair amount of scatter (Sood et al. 2007). The ratio of long timescale to orbital period ranges from 10 to 100 in these systems (WP99). In some cases the ratio is much greater, e.g., in 4U 1820–30, where the long timescale is 176 days, for an orbital period of 11 minutes (ratio 23,000). WP99 demonstrate that these periods can be explained reasonably well by a combination of disk irradiation by the central source, causing it to tilt and warp, and tidal torque from the companion, further driving the precession of this tilted disk.

To test whether the long timescale here would fit the radiative precession model, we can use Equations (17)–(19) of WP99, provided we know the properties of J1621 well enough. From the IR data, the orbital period is estimated to be in the range 3–20 hr (A. Bahramian et al. 2019, in preparation), implying that the companion is low mass and on or just beyond the main sequence, and we thus infer a companion mass in the range 0.3–1 M_\odot . The accretor is an NS, for which we assume a mass of 1.4 M_\odot . The X-ray luminosity, assuming an upper limit to the distance of 5 kpc derived from IR data (A. Bahramian et al. 2019, in preparation), is in the range $(0.45\text{--}5.98) \times 10^{36}$ erg s⁻¹. Making the same assumptions as WP99 for the outer disk radius, we can compute the radiative precession period of the disk in this system to be

$$P_\Gamma = 82 \text{ days } \alpha_{-1}^{-4/5} \left(\frac{\epsilon}{0.2} \right)^{-1} L_{X,36.5}^{-0.3} \left(\frac{P_{\text{orb}}}{12 \text{ hr}} \right)^{2/3} \left(\frac{M_T}{2 M_\odot} \right)^{1/3}. \quad (2)$$

Here numerical subindices indicate logarithms of normalization values. We have chosen standard NS values $M = 1.4 M_\odot$, $R = 10$ km, corresponding to an accretion efficiency $\epsilon = 0.2$ to convert between X-ray luminosity and mass accretion rate, and normalized to middle-of-range values for the X-ray luminosity, orbital period, and total mass of the system. We see that for reasonable values of the system parameters, the 82 day radiative precession period we predict is close to the observed long timescale modulation of 78 days. This result supports a super-orbital period as the underlying model for the observed light-curve modulation.

We thank the anonymous referee, whose comments improved the quality of this work. N.G., C.K., and P.B. acknowledge support from *Chandra* award number GO8-19061X and *Swift* award number NNH16ZDA001N-SWIFT.

The IRSF project is supported by the Grants-in-Aid for Scientific Research on Priority Areas (A) (No. 10147207 and No. 10147214). H.N. acknowledges support from a Grant-in-Aid for Scientific Research (No. 16K05301). The Australia Telescope Compact Array is part of the Australia Telescope National Facility which is funded by the Australian Government for operation as a National Facility managed by CSIRO. Special thanks go to Nobuyuki Kawai, Christina Gilligan, and Jill Neeley for their indispensable roles in data acquisition for this project. D.H. acknowledges support from the DIRAC Institute in the Department of Astronomy at the University of Washington. The DIRAC Institute is supported through generous gifts from the Charles and Lisa Simonyi Fund for Arts and Sciences, and the Washington Research Foundation. This work made use of data from the *NuSTAR* mission, a project led by the California Institute of Technology, managed by the Jet Propulsion Laboratory, and funded by the National Aeronautics and Space Administration. This research has made use of the *NuSTAR* Data Analysis Software (NuSTARDAS) jointly developed by the ASI Science Data Center (ASDC, Italy) and the California Institute of Technology (USA). We thank all operations, software and calibration teams contributing to the facilities used in this study for support with the execution and analysis of these observations.

Facilities: *Swift*, *Chandra*, *NuSTAR*, *NICER*, *MAXI*, *INTEGRAL*, *ATCA*, *IRSF*, *Gemini*, *ADS*, *HEASARC*.

Software: *MIRIAD* (Sault et al. 1995), *Stingray* (Huppenkothen et al. 2016, 2019), *emcee* (Foreman-Mackey et al. 2013), *CIAO* (v4.9.3; Fruscione et al. 2006), *HEASoft* (v624; HEASARC 2014), *XSPEC* (v12.10.0; Arnaud 1996).

Appendix Spectral Simulations Plots

We performed extensive simulations following the procedure described in Appendix A.1. of Guiriec et al. (2013) for the two best spectral models, *xillver*+*BB* and *cutoff PL*+*BB*+*Lorentzian*. By performing these simulations, we tested our ability to recover the accurate spectral parameters, i.e., those used to create the simulations. For each model we produced 105 synthetic spectra (using model parameters from Table 4) with the *FAKEIT* command in *XSPEC* V12.10.0; each synthetic spectrum was fitted with the same model used to produce it. For each parameter, we expected the probability distribution function (pdf) to peak close to the parameter value used to, produce the synthetic spectrum. To reduce computational time, we synthesized spectra using the *NuSTAR* aspect correction, the background spectrum, *rmf*, and *arf* files from *CHU 2* from the *NuSTAR* *FPMA* in Observation 15. The other spectra vary only by a multiplicative constant, which reflects the different combinations of *CHU* and *FPMs*.

The pdf of each parameter for the models discussed above are plotted in Figures 10 and 11. However, some parameters of the *xillver*+*BB* model showed evidence of jumps (discontinuities). In the Fe abundance (*A*_{Fe}) and *E*_{cut}, this is indicative of the grid of models not encompassing enough of the parameter space, shown by an excess at the edge(s) of the distributions, which are otherwise relatively smooth (Figure 10). In probability distributions with this issue, we truncated the distribution by removing these bins. We then redistributed the probability in the removed bins to the

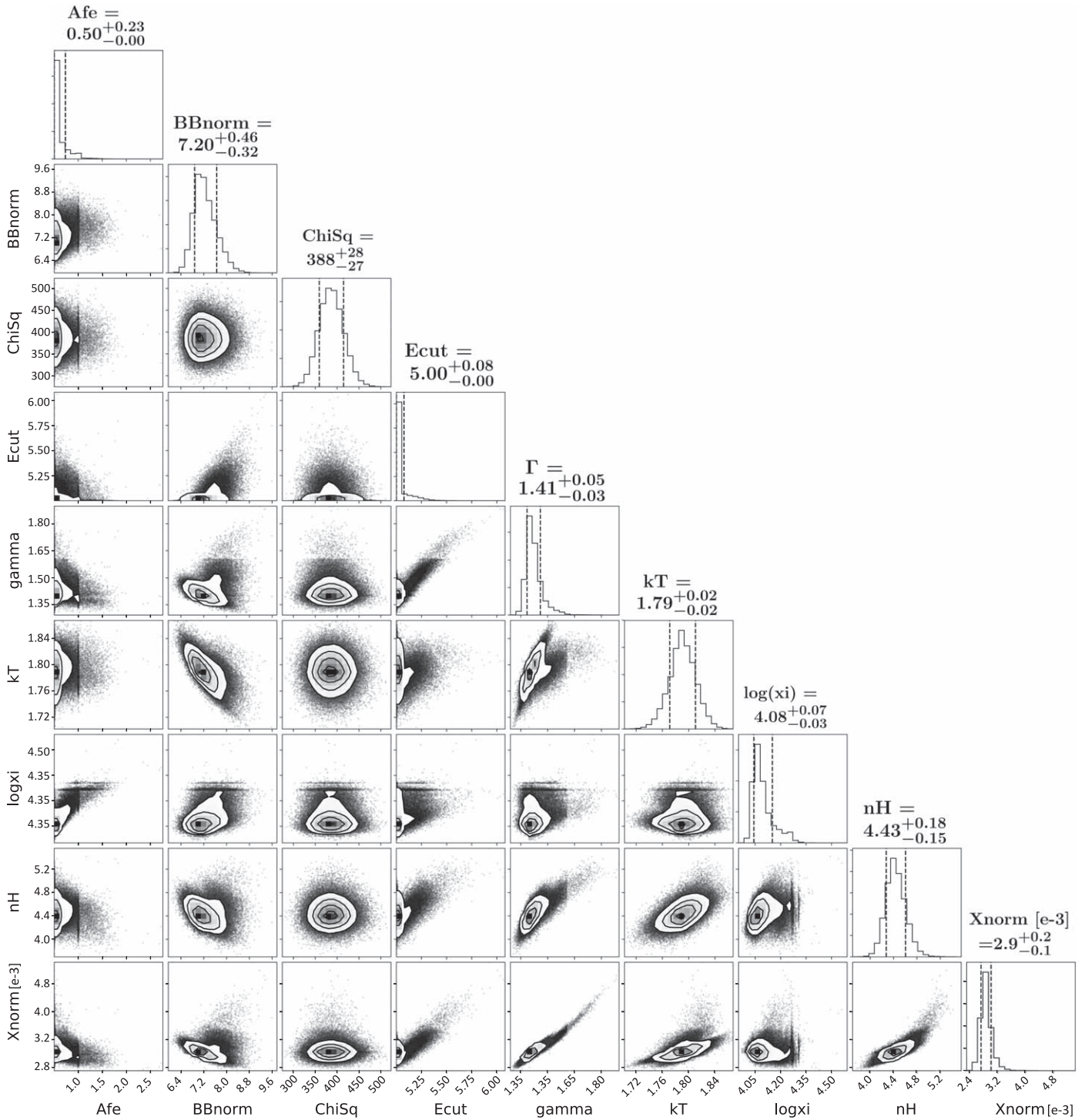


Figure 10. Parameters for 10^5 simulated spectra using an absorbed reflection spectrum plus blackbody model. Contours are at the volumetric 1σ level, 19.7% to either side of the centroid.

remaining smooth distribution, weighted with respect to the remaining bins' probability.

For both models, we calculated for each pdf the minimum and the maximum parameter values, which enclose the $\sim 68\%$ confidence interval as follows. From either side of each parameter probability distribution (rightmost tiles in Figures 10 and 11), we calculated the cumulative distribution until its value surpassed 0.16. We then chose the previous half bin that

did not surpass this value in order to denote the beginning of the $\sim 68\%$ confidence interval; the resulting confidence intervals are reported in column 6 of Table 10. These results tend to favor the cutoff PL+BB+Lorentzian model because: (a) all input parameters were recovered within the central $\sim 68\%$ confidence interval, and (b) the parameter probability distributions were smooth, indicating an adequately broad grid of parameter values.

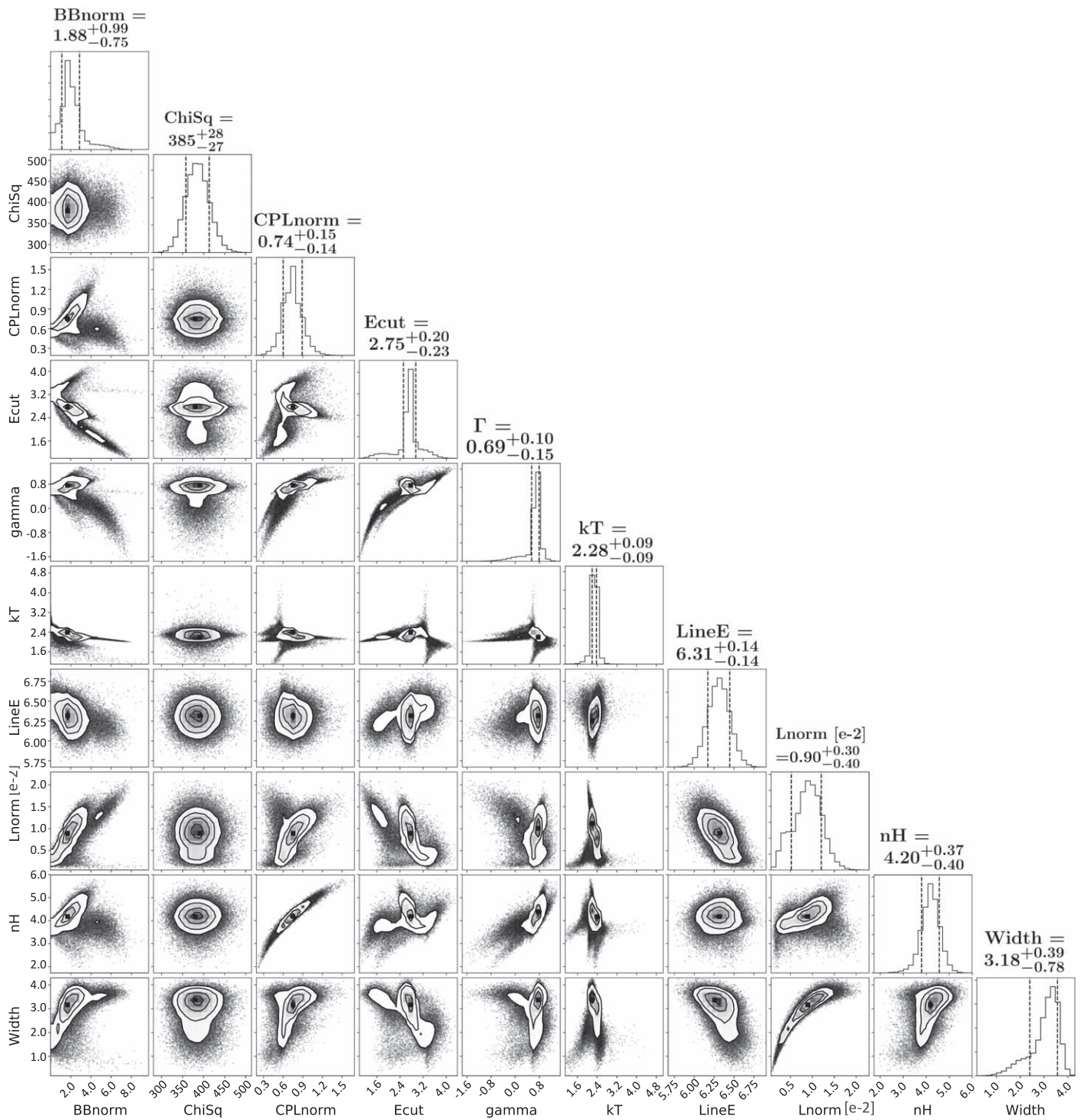


Figure 11. Parameters for 10^5 simulated spectra using an absorbed cutoff PL plus BB plus a Lorentzian. Contours are at the volumetric 1σ level, 19.7% to either side of the centroid.

Table 10
Simulation Results (*top*) Using the Absorbed Xillver + BB Model (*bottom*) Using the Absorbed Cutoff PL + BB + Lorentzian Model

Model	Parameter	Input	Min Value	Max Value	Conf. Interval (%)	Includes Input
CPL+BB+L	nH ($E+22 \text{ cm}^{-2}$)	4.23	3.84	4.58	69	✓
	Γ	0.69	0.57	0.79	69	✓
	Ecut [keV]	2.77	2.55	2.96	70	✓
	CPLnorm	0.75	0.61	0.89	70	✓
	kT [keV]	2.32	2.23	2.37	72	✓
	BB norm	1.70	1.21	2.91	69	✓
	LineE [keV]	6.31	6.18	6.45	68	✓
	Width [keV]	3.15	2.43	3.58	69	✓
	Lnorm (E-3)	8.72	5.39	12.09	69	✓
Xillver+BB	nH ($E22 \text{ cm}^{-2}$)	4.39	4.28	4.61	70	✓
	Γ	1.40	1.39	1.46	71	✓
	Afe	0.50	0.58	0.94	72	×
	Ecut [keV]	5.00	5.04	5.23	69	×
	logxi	4.05	4.05	4.15	70	✓
	Xnorm (E-3)	2.84	2.75	3.01	71	✓
	kT [keV]	1.79	1.77	1.81	69	✓
	BB norm	6.99	6.91	7.67	70	✓

Note. Column 7 denotes if the confidence interval from column 6 includes the input value used to create the synthetic spectra.

ORCID iDs

Nicholas M. Gorgone  <https://orcid.org/0000-0002-1653-6411>

Chryssa Kouveliotou  <https://orcid.org/0000-0003-1443-593X>

Ralph A. M. J. Wijers  <https://orcid.org/0000-0002-3101-1808>

Enrico Bozzo  <https://orcid.org/0000-0002-7504-7423>

Sylvain Guiriec  <https://orcid.org/0000-0001-5780-8770>

Daniela Huppenkothen  <https://orcid.org/0000-0002-1169-7486>

Ersin Göğüş  <https://orcid.org/0000-0002-5274-6790>


Arash Bahramian  <https://orcid.org/0000-0003-2506-6041>

Jamie Kennea  <https://orcid.org/0000-0002-6745-4790>

Justin D. Linford  <https://orcid.org/0000-0002-3873-5497>

James Miller-Jones  <https://orcid.org/0000-0003-3124-2814>

Paz Beniamini  <https://orcid.org/0000-0001-7833-1043>


Deepto Chakrabarty  <https://orcid.org/0000-0001-8804-8946>

Jonathan Granot  <https://orcid.org/0000-0001-8530-8941>

Dieter H. Hartmann  <https://orcid.org/0000-0002-8028-0991>

Daniel Stern  <https://orcid.org/0000-0003-2686-9241>

John A. Tomsick  <https://orcid.org/0000-0001-5506-9855>

Alexander J. van der Horst  <https://orcid.org/0000-0001-9149-6707>

George A. Younes  <https://orcid.org/0000-0002-7991-028X>

References

An, H., Madsen, K. K., Westergaard, N. J., et al. 2014, *Proc. SPIE*, 9144, 91441Q

Arnaud, K. A. 1996, in ASP Conf. Ser. 101, *Astronomical Data Analysis Software and Systems V*, ed. G. H. Jacoby & J. Barnes (San Francisco, CA: ASP), 17

Bachetti, M., Harrison, F. A., Cook, R., et al. 2015, *ApJ*, 800, 109

Bachetti, M., & Huppenkothen, D. 2018, *ApJL*, 853, L21

Bahramian, A., Kennea, J. A., Evans, P. A., et al. 2018, *ATel*, 10874

Bult, P., Altamirano, D., Arzoumanian, Z., et al. 2018a, *ApJ*, 860, L9

Bult, P., Arzoumanian, Z., Cackett, E. M., et al. 2018b, *ApJ*, 859, L1

Bult, P., Gorgone, N., Younes, G., Kouveliotou, C., & Harrison, F. 2017, *ATel*, 11067

Burrows, D. N., Hill, J. E., Nousek, J. A., et al. 2005, *SSRv*, 120, 165

Chelovekov, I. V., Grebenev, S. A., Mereminskiy, I. A., & Prosvetov, A. V. 2017, *AstL*, 43, 781

Chenevez, J., Alizai, K., Lepingwell, V. A., et al. 2018, *ATel*, 11272

Christian, D. J., & Swank, J. H. 1997, *ApJS*, 109, 177

Courvoisier, T., Walter, R., Beckmann, V., et al. 2003, *A&A*, 411, L53

Done, C., Gierliński, M., & Kubota, A. 2007, *A&ARv*, 15, 1

Eikenberry, S. S., Elston, R., Raines, S. N., et al. 2004, *Proc. SPIE*, 5492, 1196

Evans, P. A., Beardmore, A. P., Page, K. L., et al. 2009, *MNRAS*, 397, 1177

Foreman-Mackey, D., Hogg, D. W., Lang, D., & Goodman, J. 2013, *PASP*, 125, 306

Fruscione, A., McDowell, J. C., Allen, G. E., et al. 2006, *Proc. SPIE*, 6270, 62701V

Galloway, D. K., & Keek, L. 2017, arXiv:1712.06227

García, J., Dauser, T., Lohfink, A., et al. 2014, *ApJ*, 782, 76

Gendreau, K. C., Arzoumanian, Z., Adkins, P. W., et al. 2016, *Proc. SPIE*, 9905, 99051H

Gerend, D., & Boynton, P. E. 1976, *ApJ*, 209, 562

Glass, I. S., & Nagata, T. 2000, *MNSSA*, 59, 110

Goad, M. R., Tyler, L. G., Beardmore, A. P., et al. 2007, *A&A*, 476, 1401

Gorgone, N., Kouveliotou, C., & Baring, M. 2017a, *AAS/Meeting*, 16, 105.22

Gorgone, N., Kouveliotou, C., Younes, G., & Kennea, J. 2018, *ATel*, 11317

Gorgone, N., Younes, G., Kouveliotou, C., et al. 2017b, *ATel*, 10969

Guiriec, S., Daigne, F., Hascoët, R., et al. 2013, *ApJ*, 770, 32

Güver, T., Özel, F., Cabrera-Lavers, A., & Wroblewski, P. 2010, *ApJ*, 712, 964

Harrison, F. A., Craig, W. W., Christensen, F. E., et al. 2013, *ApJ*, 770, 103

Hashimoto, T., Negoro, H., Ueno, S., et al. 2017, *ATel*, 10869

Huppenkothen, D., Bachetti, M., Stevens, A. L., et al. 2019, *ApJ*, 881, 39

Huppenkothen, D., Bachetti, M., Stevens, A. L., Migliari, S., & Balm, P. 2016, *Stingray: Spectral-timing software*, *Astrophysics Source Code Library*, ascl:1608.001

Kouveliotou, C., Meegan, C. A., Fishman, G. J., et al. 1993, *ApJ*, 413, L101

Lebrun, F., Leray, J. P., Lavocat, P., et al. 2003, *A&A*, 411, L141

Lepingwell, V. A., Fiocchi, M., Chenevez, J., et al. 2018, *ATel*, 11252

Lewin, W. H. G., van Paradijs, J., & Taam, R. E. 1993, *SSRv*, 62, 223

Lund, N., Budtz-Jørgensen, C., Westergaard, N. J., et al. 2003, *A&A*, 411, L231

Matsuoka, M., Kawasaki, K., Ueno, S., et al. 2009, *PASJ*, 61, 999

Mihara, T., Nakajima, M., Sugizaki, M., et al. 2011, *PASJ*, 63, S623

Mitsuda, K., Inoue, H., Nakamura, N., & Tanaka, Y. 1989, *PASJ*, 41, 97

Morii, M., Yamaoka, H., Mihara, T., Matsuoka, M., & Kawai, N. 2016, *PASJ*, 68, S11

Murray, S. S., Austin, G. K., Chappell, J. H., et al. 2000, *Proc. SPIE*, 4012, 68

Nagashima, C., Nagayama, T., Nakajima, Y., et al. 1999, in *Star Formation*, ed. T. Nakamoto (Nagano: Nobeyama Radio Observatory), 397

Nagayama, T., Nagashima, C., Nakajima, Y., et al. 2003, *Proc. SPIE*, 4841, 459

Negoro, H., Kohama, M., Serino, M., et al. 2016, *PASJ*, 68, S1

Prigozhin, G., Gendreau, K., Foster, R., et al. 2012, *Proc. SPIE*, 8453, 845318

- Remillard, R. A., & McClintock, J. E. 2006, *ARA&A*, **44**, 49
- Romano, P., Campana, S., Chincarini, G., et al. 2006, *A&A*, **456**, 917
- Roming, P. W. A., Hunsberger, S. D., Nousek, J. A., et al. 2004, in AIP Conf. Ser. 727, *Gamma-Ray Bursts: 30 Years of Discovery*, ed. E. Fenimore & M. Galassi (Melville, NY: AIP), 651
- Rybicki, G. B., & Lightman, A. P. 1979, *Radiative Processes in Astrophysics* (New York: Wiley)
- Sault, R. J., Teuben, P. J., & Wright, M. C. H. 1995, in ASP Conf. Ser. 77, *Astronomical Data Analysis Software and Systems IV*, ed. R. A. Shaw, H. E. Payne, & J. J. E. Hayes (San Francisco, CA: ASP), 433
- Skrutskie, M. F., Cutri, R. M., Stiening, R., et al. 2006, *AJ*, **131**, 1163
- Sood, R., Farrell, S., O'Neill, P., & Dieters, S. 2007, *AdSpR*, **40**, 1528
- Titarchuk, L. 1994, *ApJ*, **434**, 570
- Tomida, H., Tsunemi, H., Kimura, M., et al. 2011, *PASJ*, **63**, 397
- Ubertini, P., Lebrun, F., Di Cocco, G., et al. 2003, *A&A*, **411**, L131
- van der Klis, M. 1989, *NATO Advanced Sci. Inst. Ser. C*, **262**, 27
- Vaughan, S. 2010, *MNRAS*, **402**, 307
- Verner, D. A., Ferland, G. J., Korista, K. T., & Yakovlev, D. G. 1996, *ApJ*, **465**, 487
- Wijers, R. A. M. J., & Pringle, J. E. 1999, *MNRAS*, **308**, 207
- Wilms, J., Allen, A., & McCray, R. 2000, *ApJ*, **542**, 914
- Wilson, W. E., Ferris, R. H., Axtens, P., et al. 2011, *MNRAS*, **416**, 832